Computer Methods in Applied Mechanics and Engineering 457 (2026) 118971

Contents lists available at ScienceDirect

Computer Methods in Applied Mechanics and Engineering

journal homepage: www.elsevier.com/locate/cma

# Multiscale isogeometric topology optimization for fatigue-resistant lattice materials with additive manufacturing-induced geometric defects

Jinyu Gu [a,b], Yingjun Wang [a,*], Hang Xu [b,*]

[a] National Engineering Research Center of Novel Equipment for Polymer Processing, The Key Laboratory of Polymer Processing Engineering of the Ministry of Education, Guangdong Provincial Key Laboratory of Technique and Equipment for Macromolecular Advanced Manufacturing, South China University of Technology, Guangzhou 510641, China

[b] Department of Mechanical, Industrial and Aerospace Engineering, Concordia University, Montreal, QC H3A 0C3, Canada

## HIGHLIGHTS

- Developed a multiscale isogeometric topology optimization method for fatigue design.
- The proposed framework incorporates microscale high-cycle fatigue damage constraints.
- Considered lattice materials with additive manufacturing-induced geometric defects.
- Enhanced fatigue resistance of structures filled with different defective lattices.
- Verified the effectiveness of the framework through 2D and 3D numerical examples.

## GRAPHICAL ABSTRACT

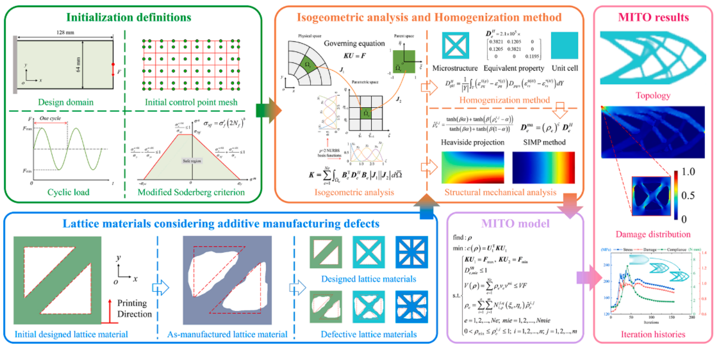


## ARTICLE INFO

*Keywords:*
Isogeometric topology optimization
Fatigue damage
Lattice materials
Microscale fatigue damage
Soderberg criterion
Goodman criterion

## ABSTRACT

Lattice materials are being widely adopted for cyclic load-bearing applications, such as lattice hip implants. However, metal additive manufacturing-induced geometric defects and material imperfections act as stress raisers, strongly affecting their fatigue resistance. This study optimizes the fatigue resistance of structures made of defective lattice materials by introducing a multiscale isogeometric topology optimization (MITO) framework, which incorporates microscale fatigue damage constraints into the optimization process. The optimization objective is to minimize the structural compliance, subject to a global volume constraint and a worst-case microscale fatigue damage constraint aggregated via a modified $p$-norm function. The high-cycle fatigue damage of

* Corresponding authors.
*E-mail addresses:* wangyj84@scut.edu.cn (Y. Wang), hang.xu@concordia.ca (H. Xu).

https://doi.org/10.1016/j.cma.2026.118971
Received 7 January 2026; Received in revised form 31 March 2026; Accepted 4 April 2026
Available online 10 April 2026

defective lattice materials is evaluated via the modified Soderberg criterion. To achieve clear and well-defined topology boundaries, a Heaviside projection scheme is embedded into the material interpolation model based on the solid isotropic material with penalization (SIMP) method. The sensitivities of the fatigue damage constraint with respect to the design variables are derived using the adjoint method, and the optimization is solved via the Method of Moving Asymptotes (MMA). Numerical examples of 2D and 3D benchmark structures with various defective lattice materials under different loading amplitudes demonstrate the robustness and effectiveness of the proposed method. The framework is further extended to incorporate the modified Goodman criterion, verifying its applicability under different fatigue evaluation models. The presented method offers an efficient design route for fatigue-resistant optimization of defective lattices.

## 1. Introduction

Lattice materials can alter and achieve superior properties beyond those of base materials through a rational structural design. They offer promising strategies for structural-functional integration and performance enhancement by achieving desirable properties such as high specific strength and excellent energy absorption capacity, while minimizing material consumption [1–3]. Lattice materials thus have widespread applications in aerospace [4,5], biomedical [6,7], automotive [8], and building [9,10] sectors.

Ongoing advances in additive manufacturing (AM) technologies, such as selective laser melting (SLM), facilitate the fabrication of lattice materials [11–13]. For instance, titanium lattice structures fabricated by metal AM have been applied in customized hip implants [14]. However, unavoidable process-induced imperfections often result in geometric deviations from the intended design, leading to unexpected variations in mechanical and functional performance [15,16]. Notably, such deviations can significantly degrade the fatigue performance of lattice structures, primarily due to the pronounced stress concentrations caused by the non-uniform material distribution inherent in AM processes [17,18]. For example, considering the periodic nature of human gait, fatigue resistance is a critical aspect of lattice hip implants. AM-induced geometric defects and material imperfections, such as surface irregularities and internal pores generated via SLM, act as stress raisers, strongly affecting the fatigue resistance of lattice hip implants, posing a potential risk for overall structural failure [19]. It is thus essential to incorporate the microscale fatigue behavior of defect-containing lattice materials into structural design frameworks.

The high cost of fatigue characterization in terms of time and number of specimens draws towards the development of numerical techniques to predict the fatigue behavior and design AM lattice structures. Nevertheless, in comparison to the vast amount of literature published on the static mechanical behavior of lattices [20–22], few studies on their fatigue resistance have been published. Hedayati et al. [23] described a numerical simulation-based method considering stress concentration factor due to the joints and geometrical irregularities (roughness and variations in the cross-section of the cell-walls) to estimate the fatigue life of porous structures. Additional multiscale numerical design methods for the fatigue life of defective lattices require further investigation.

Among various structural design strategies, topology optimization (TO) has emerged as an innovative, performance-driven methodology for structural design [24–26]. Currently, various TO methods have been developed to address fatigue damage and have been successfully applied to structural fatigue-resistant design [27–29]. Existing research in fatigue-constrained topology optimization (FCTO) can be broadly categorized into two classes based on the loading conditions: proportional [30] and non-proportional loading [31]. Under proportional loading, commonly employed fatigue criteria include the Lemaitre damage law [32], the Crossland criterion [33], the Gerber criterion [34], and the Soderberg criterion [35]. For example, Gu et al. [36] introduced an isogeometric topology optimization (ITO) framework by means of the Soderberg criterion. Ni et al. [37] applied the Goodman criterion to evaluate fatigue damage in microstructures and proposed a bi-scale topology optimization method. For non-proportional loading, most studies are on the basis of the Palmgren-Miner linear damage accumulation rule [31] and the Morrow nonlinear fatigue model [38]. Lee et al. [39] developed a TO method for fatigue constraints under variable amplitude loading using the Palmgren-Miner rule. Ye et al. [40] developed an FCTO method for orthotropic materials under non-proportional cyclic loads. Gu et al. [38] further addressed nonlinear fatigue accumulation arising from load interaction using the Morrow criterion. Moreover, FCTO methods have also been applied to various structural optimization problems, including AM [41], compliant mechanisms [42], and composite materials [43]. However, most existing FCTO methods focus on macrostructural design, with limited attention to integrating microscale fatigue damage within the macrostructural optimization framework.

To enhance global structural performance by harnessing capabilities of microstructures, e.g. lattices, the application of multiscale topology optimization (MTO) has attracted considerable attention [44,45] in a wide range of sectors, including structural statics [46, 47], heat conduction [48,49], structural dynamics [50,51], and buckling analysis [52,53]. Most MTO methods in literature rely on conventional finite element analysis (FEA). Conventional FEA faces inherent limitations in handling complex geometries, maintaining inter-element continuity, and achieving accurate interpolation under highly refined meshes. To overcome this deficiency, Hughes et al. [54]. introduced the isogeometric analysis (IGA) method, which employs Non-Uniform Rational B-Splines (NURBS) to represent both geometry and physical fields within a unified formulation. IGA offers exact geometry representation, superior continuity (e.g. $C^1$, $C^2$), and enhanced numerical stability [55], making it particularly well-suited for multiscale analysis of microstructure materials where accuracy and smoothness are critical. The IGA-based TO framework for conducting multiscale structural design [56,57], i.e. multiscale isogeometric topology optimization (MITO) method, has been developed [58–60].

However, most existing MITO methods neglect geometric imperfections of structures introduced during the manufacturing process. While these optimized structures may display good performance under nominal working conditions, they are often susceptible to premature failure when subjected to slight geometric deviations or minor load perturbations, thus limiting their applicability in real-world scenarios. In practice, metallic lattice structures fabricated via AM inherently suffer from geometric defects due to process-induced inaccuracies, leading to discrepancies between the as-built and as-designed geometries. These defects can dramatically alter the local stress distribution within the metallic lattice and consequently degrade its fatigue performance [18,61]. To address such issues, studies in literature have incorporated uncertainties in geometry and material properties into the optimization framework to enhance the robustness of structural designs [62–64]. However, the impact of AM-induced geometric defects in the metal lattice on fatigue damage behavior and their integration into TO models remains unexplored and warrants further investigation.

This study aims to develop an MITO method that incorporates microscale fatigue damage constraints of defective lattice materials, specifically targeting high-cycle fatigue life enhancement for structures embedded with predefined lattice configurations. The mathematical framework of the MITO is formulated to minimize structural compliance while accounting for both microscale fatigue damage and global volume constraints. A worst-case fatigue damage evaluation strategy is employed in conjunction with a modified $p$-norm aggregation function to address the computational complexity arising from extensive microscale constraints. The study presents a detailed derivation of the sensitivity analysis for the fatigue damage constraint function. With effectiveness demonstrated through 2D and 3D numerical examples, the proposed framework provides a scalable method for integrating microscale fatigue behavior into macrostructural topology optimization.

The remainder of the paper is organized as follows. Section 2 presents the fundamental theory of IGA. Section 3 elaborates on the IGA-based fatigue damage assessment method for lattice materials. Section 4 presents the mathematical model and implementation framework of the proposed MITO method, taking into account the microscale fatigue damage constraints. Section 5 demonstrates the effectiveness and feasibility of the proposed method through numerical examples in 2D and 3D. Section 6 concludes this study and provides insights into future research.

## 2. Isogeometric analysis

In this section, the fundamentals of NURBS are briefly reviewed in Section 2.1. In addition, Section 2.2 introduces the IGA theory represented by the NURBS, which serves as the analytical foundation for the subsequent multiscale optimization framework.

### 2.1. NURBS fundamental theory

NURBS is one of the standard tools for curve and surface modeling, and it is widely used in computer-aided design (CAD) and computer graphics. It is constructed based on B-spline functions. The 1D B-spline basis function $B_{i,p}(\xi)$ is defined recursively using the Cox-de Boor formula as follows [54,65]:

$$B_{i,p}(\xi) = \begin{cases} 1, & \text{if } \xi_i \le \xi < \xi_{i+1} \\ 0, & \text{otherwise} \end{cases}, \quad \text{for } p = 0 \tag{1}$$

$$B_{i,p}(\xi) = \frac{\xi - \xi_i}{\xi_{i+p} - \xi_i} B_{i,p-1}(\xi) + \frac{\xi_{i+p+1} - \xi}{\xi_{i+p+1} - \xi_{i+1}} B_{i+1,p-1}(\xi), \quad \text{for } p > 0 \tag{2}$$

where $p$ is the order, $\xi_i$ is $i$-th knot values with $i = 1, 2, ..., n + p + 1$, $\left[\xi_1, \xi_{n+p+1}\right]$ is a patch, $[\xi_i, \xi_{i+1})$ is the $i$-th knot span, and $\boldsymbol{\Xi} = \left\{\xi_1, \xi_2, ..., \xi_{n+p+1}\right\}$ denotes a non-decreasing knot vector, which defines the parameter space partitioning for B-spline or NURBS basis functions.

By introducing a weighting factor to the B-spline basis functions, the 1D NURBS basis function of order $p$ is defined as:

$$N_{i,p}(\xi) = \frac{B_{i,p}(\xi)\omega_i}{\sum_{j=1}^{n} B_{j,p}(\xi)\omega_j} \tag{3}$$

where $\omega_i$ denotes the weights.

Furthermore, the NURBS basis function can be extended to 2D space, and is expressed as:

$$N_{i,p}^{j,q}(\xi, \eta) = \frac{B_{i,p}(\xi)B_{j,q}(\eta)\omega_{i,j}}{\sum_{k=1}^{n}\sum_{l=1}^{m} B_{k,p}(\xi)B_{l,q}(\eta)\omega_{k,l}} \tag{4}$$

where $p$ and $q$ represent the orders of the B-spline basis functions in the $\xi$- and $\eta$-directions, respectively; $\omega_{i,j}$ is the weight value corresponding to the tensor product $B_{i,p}(\xi)B_{j,q}(\eta)$, where $B_{i,p}(\xi)$ and $B_{j,q}(\eta)$ are B-spline basis functions defined in the $\xi$- and $\eta$-directions, respectively.

A 2D NURBS surface can be constructed by introducing the control point coordinates into Eq. (4), resulting in:

$$S(\xi, \eta) = \sum_{i=1}^{n}\sum_{j=1}^{m} N_{i,p}^{j,q}(\xi, \eta)\boldsymbol{P}_{i,j} \tag{5}$$

where $\boldsymbol{P}_{i,j}$ denotes the coordinates of the control points.

### 2.2. NURBS-based isogeometric structural mechanical analysis

In conventional FEA, the computational domain is discretized into finite elements, resulting in an approximation of the original geometry. This geometric mismatch between the numerical model and the design geometry introduces discretization errors that can be alleviated through mesh refinement, albeit at the expense of substantially increased computational cost. In contrast, IGA operates directly on the exact NURBS-based geometry of CAD models, thereby eliminating geometric discretization errors [66]. This inherent advantage of IGA has been validated in literature [67–69]. Furthermore, IGA ensures higher-order continuity of displacement and stress fields across elements, which is particularly beneficial for applications such as structural fatigue analysis, where solution smoothness and precision are critical.

In IGA, the NURBS basis functions used for geometric modeling are directly employed as shape functions in numerical analysis. The governing equation for linear elastic equilibrium in structural mechanics is given by:

$$\boldsymbol{KU} = \boldsymbol{F} \tag{6}$$

where $\boldsymbol{K}$ denotes the global stiffness matrix, $\boldsymbol{U}$ is the global displacement vector, and $\boldsymbol{F}$ represents the global load vector. In IGA, the expressions for $\boldsymbol{U}$ and $\boldsymbol{K}$ are given by [70]:

$$\boldsymbol{U}(\xi,\eta) = \sum_{i=1}^{m}\sum_{j=1}^{n} N_{i,j}(\xi,\eta)\boldsymbol{u}_{i,j} \tag{7}$$

$$\begin{aligned}\boldsymbol{K} &= \sum_{e=1}^{Ne}\boldsymbol{k}_e = \sum_{e=1}^{Ne}\int_{\Omega_e}\boldsymbol{B}_e^{\mathrm{T}}\boldsymbol{D}_0\boldsymbol{B}_e d\Omega \\ &= \sum_{e=1}^{Ne}\int_{\hat{\Omega}_e}\boldsymbol{B}_e^{\mathrm{T}}\boldsymbol{D}_0\boldsymbol{B}_e|\boldsymbol{J}_1|d\hat{\Omega} = \sum_{e=1}^{Ne}\int_{\overline{\Omega}_e}\boldsymbol{B}_e^{\mathrm{T}}\boldsymbol{D}_0\boldsymbol{B}_e|\boldsymbol{J}_1||\boldsymbol{J}_2|d\overline{\Omega}\end{aligned} \tag{8}$$

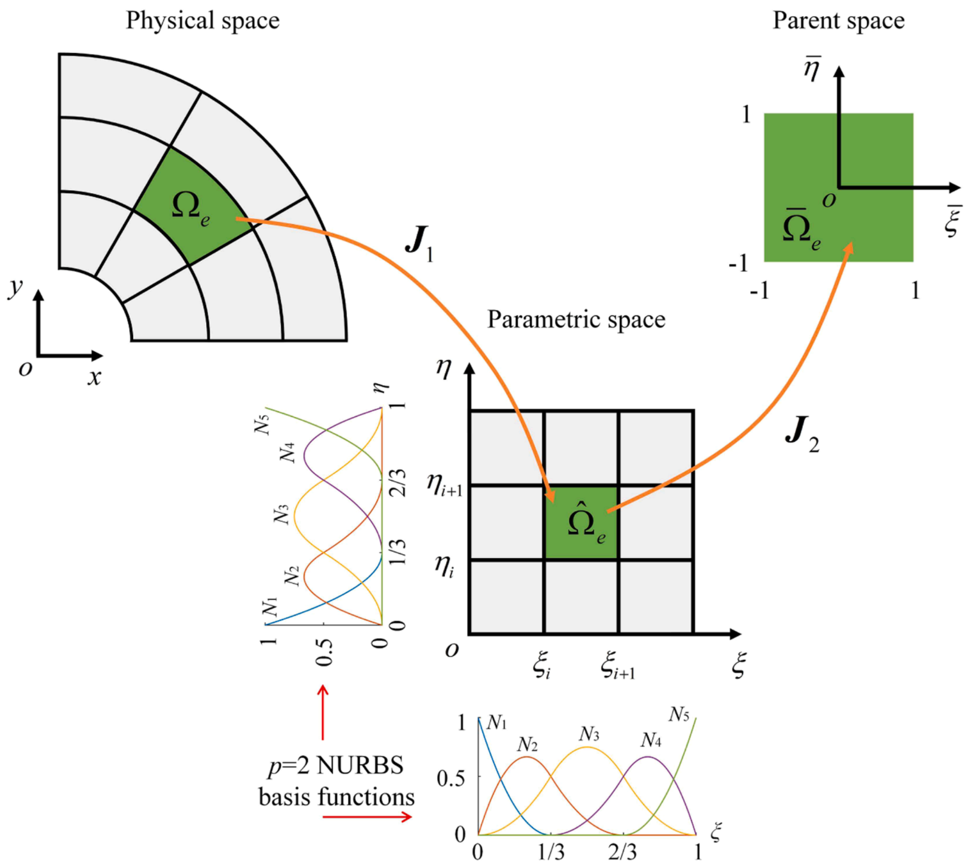


**Fig. 1.** The spatial mapping relationship for integration in IGA.

where $\boldsymbol{u}_{i,j}$ is the displacement of the control point, $\boldsymbol{k}_e$ is the stiffness matrix of element $e$, $Ne$ is the total number of elements, $\boldsymbol{B}_e$ is the constitutive matrix, $\boldsymbol{D}_0$ denotes the elasticity matrix, $\Omega_e$ is the physical space, $\widehat{\Omega}_e$ is the parameter space, $\overline{\Omega}_e$ is the parent space, $\boldsymbol{J}_1$ denotes the Jacobian matrix mapping from the physical space to the parametric space, while $\boldsymbol{J}_2$ represents the Jacobian matrix mapping from the parametric space to the parent space. Their relationship is illustrated in Fig. 1. Additional theoretical details can be found in Reference [54].

In 2D IGA framework, the stress components in each element are computed via displacement field. The von Mises equivalent stress is derived from the stress components to assess the yielding condition of the material under isotropic assumptions. The element stress tensor $\boldsymbol{\sigma}_e$ and the corresponding von Mises stress $\sigma_e^{\mathrm{vM}}$ are expressed as follows:

$$\boldsymbol{\sigma}_e = \boldsymbol{D}_0\boldsymbol{B}_e\boldsymbol{u}_e = \begin{bmatrix} \sigma_{e,x} & \sigma_{e,y} & \sigma_{e,xy} \end{bmatrix}^{\mathrm{T}} \tag{9}$$

$$\sigma_e^{\mathrm{vM}} = \sqrt{(\boldsymbol{\sigma}_e)^{\mathrm{T}}\boldsymbol{Q}\boldsymbol{\sigma}_e} \tag{10}$$

where $\boldsymbol{u}_e$ denotes the element displacement vector composed of the displacements of the associated control points, and $\sigma_{e,x}$, $\sigma_{e,y}$, $\sigma_{e,xy}$ denote the three components of the element stress; $\boldsymbol{Q}$ is the transformation matrix, and its 2D expression is given as:

$$\boldsymbol{Q} = \begin{bmatrix} 1 & -0.5 & 0 \\ -0.5 & 1 & 0 \\ 0 & 0 & 3 \end{bmatrix} \tag{11}$$

## 3. Fatigue damage analysis of lattice materials based on isogeometric analysis

High-cycle (with loading cycles exceeds $10^7$) fatigue damage occurs at low stress, usually within the material's elastic range and below the yielding stress. Therefore, high-cycle fatigue analysis is generally formulated based on linear elastic theory and the structure experiences negligible plastic deformation throughout its service life. This section focuses on the theoretical formulation of lattice material fatigue analysis in the framework of linear elastic IGA. Section 3.1 describes the modified Soderberg criterion, which is widely used in evaluating fatigue safety in the elastic domain. Section 3.2 outlines a homogenization-based multiscale framework for fatigue analysis of lattice materials, providing a foundation for incorporating multiscale fatigue damage constraints into the MITO method. Section 3.3 designs lattice materials considering additive manufacturing defects and calculates the corresponding homogenized material properties.

### 3.1. Soderberg criterion

Fig. 2(a) illustrates a proportional cyclic load, and the resulting stress state evolution is shown in Fig. 2(b). Under proportional cyclic loading, the stress state at any location in the structure is defined as follows:

$$\begin{cases} \sigma_e^a = \dfrac{(\sigma_e)_{\max} - (\sigma_e)_{\min}}{2} \\ \sigma_e^m = \dfrac{(\sigma_e)_{\max} + (\sigma_e)_{\min}}{2} \end{cases} \tag{12}$$

where $\sigma_e^a$ is the stress amplitude, $\sigma_e^m$ is the mean stress, $(\sigma_e)_{\max}$ and $(\sigma_e)_{\min}$ represent the maximum and minimum stresses under cyclic loading, respectively.

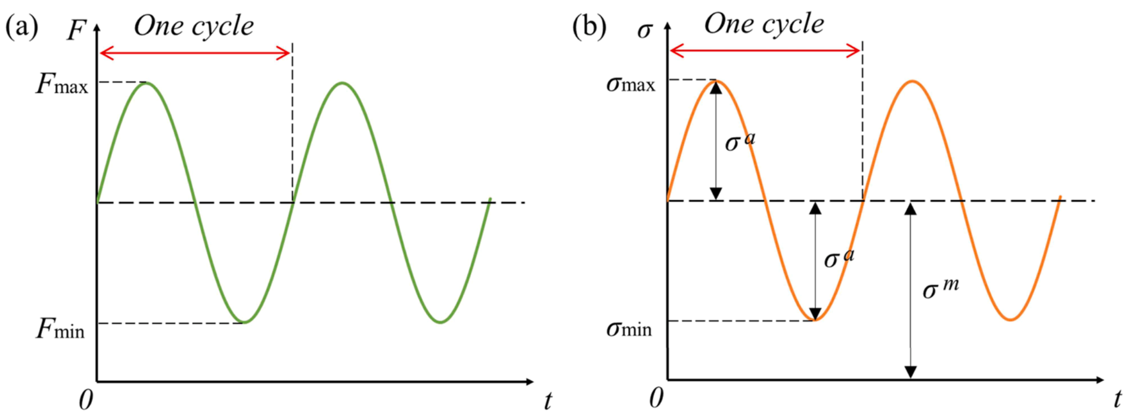


**Fig. 2.** The proportional cyclic load history: (a) load and (b) stress.

Within the linear elastic regime, the stress amplitude and mean stress can be computed from the maximum (or minimum) load results by introducing appropriate scaling factors [34,71]. Accordingly, the stress amplitude vector and the mean stress vector are given as follows:

$$\begin{cases} \boldsymbol{\sigma}_e^a = c^a \boldsymbol{\sigma}_e \\ \boldsymbol{\sigma}_e^m = c^m \boldsymbol{\sigma}_e \end{cases} \tag{13}$$

where $c^a$ and $c^m$ are the scaling factors for stress amplitude and mean stress, respectively. For linear elasticity problems, the formulas for $c^a$ and $c^m$ are as follows:

$$\begin{cases} c^a = \dfrac{1-(F_{\min}/F_{\max})}{2} \\ c^m = \dfrac{1+(F_{\min}/F_{\max})}{2} \end{cases} \tag{14}$$

As defined in Eq. (10), the equivalent stress amplitude $\sigma_e^{a,\mathrm{vM}}$ and mean stress $\sigma_e^{m,\mathrm{vM}}$ for element $e$ are calculated adopting the von Mises stress criterion, as follows:

$$\begin{cases} \sigma_e^{a,\mathrm{vM}} = \sqrt{\left(\boldsymbol{\sigma}_e^a\right)^{\mathrm{T}} \mathbf{Q} \boldsymbol{\sigma}_e^a} \\ \sigma_e^{m,\mathrm{vM}} = \sqrt{\left(\boldsymbol{\sigma}_e^m\right)^{\mathrm{T}} \mathbf{Q} \boldsymbol{\sigma}_e^m} \end{cases} \tag{15}$$

In literature, several classical models are widely used to evaluate uniaxial high-cycle fatigue damage, including the Gerber, Goodman, ASME Elliptic, and Soderberg criteria [34,35,72]. Among these, the Soderberg criterion is the most conservative, imposing the strictest constraints on allowable stress combinations. In contrast, the other three criteria allow for a broader design domain, which generally results in a reduced safety margin. To account for all potential damage scenarios in a conservative manner, the Soderberg criterion is adopted in this study:

$$D_e^{SB} = \frac{\sigma_e^{a,\mathrm{vM}}}{\sigma_{Nf}} + \frac{\sigma_e^{m,\mathrm{vM}}}{\sigma_y} \leq 1 \tag{16}$$

where $\sigma_y$ denotes the yield tensile stress and $\sigma_{Nf}$ represents the stress amplitude below which a metallic material is expected to withstand an infinite number of loading cycles without failure. The stress $\sigma_{Nf}$ can be estimated using the Basquin equation, which characterizes the S-N relationship (where S refers to the stress amplitude and N is the number of cycles to failure) [38]:

$$\sigma_{Nf} = \sigma'_f \left(2N_f\right)^b \tag{17}$$

where $\sigma'_f$ is the fatigue strength coefficient, $N_f$ is the number of load reversals, and $b$ is the fatigue strength exponent of the material.

It is worth noting that metallic materials are generally resistant to fatigue damage under compressive stress, as compression tend to suppress crack initiation and propagation. However, when compressive stresses become significant, structural yielding may occur, necessitating the special consideration of cases where the mean stress is negative (i.e., dominated by compressive loading). Taking these factors into account, the fatigue constraint of the modified Soderberg criterion is reformulated as follows [30]:

$$D_e^{SB} = \begin{cases} \dfrac{\sigma_e^{a,\mathrm{vM}}}{\sigma_{Nf}} + \dfrac{\sigma_e^{m,\mathrm{vM}}}{\sigma_y} \leq 1, \sigma_e^{m,\mathrm{vM}} \geq 0 \\ \dfrac{\sigma_e^{a,\mathrm{vM}}}{\sigma_y} - \dfrac{\sigma_e^{m,\mathrm{vM}}}{\sigma_{yc}} \leq 1, \sigma_e^{m,\mathrm{vM}} \leq \left(\dfrac{\sigma_{Nf}}{\sigma_y} - 1\right)\sigma_{yc} \\ \dfrac{\sigma_e^{a,\mathrm{vM}}}{\sigma_{Nf}} \leq 1, \left(\dfrac{\sigma_{Nf}}{\sigma_y} - 1\right)\sigma_{yc} < \sigma_e^{m,\mathrm{vM}} < 0 \end{cases} \tag{18}$$

where $\sigma_{yc}$ represents the yield compressive stress of the material.

Since the von Mises stress is always non-negative, it cannot directly distinguish between tensile and compressive loading conditions. To this end, the sign of the maximum absolute principal stress is adopted to determine whether the external loading is in tension or compression. Accordingly, the signed von Mises mean stress is reformulated as follows:

$$\sigma_e^{m,\mathrm{vM}} = \mathrm{sign} \cdot \sqrt{\left(\boldsymbol{\sigma}_e^m\right)^{\mathrm{T}} \mathbf{Q} \boldsymbol{\sigma}_e^m} \tag{19}$$

where "sign" denotes the sign function, which takes a value of 1 for tensile stress ($|\sigma_{e,1}^m| \geq |\sigma_{e,3}^m|$) and $-1$ for compressive stress ($|\sigma_{e,1}^m| < |\sigma_{e,3}^m|$), $\sigma_{e,1}^m$ and $\sigma_{e,3}^m$ are the sorted principal mean stresses. The fatigue diagram corresponding to the above fatigue constraints is illustrated in Fig. 3. The region satisfying the aforementioned constraints (defined by the combination of stress amplitude and mean stress) is referred to as the safe region. This was not considered in our previous studies [36], which, in contrast, the mean stresses calculated by the von Mises stress method equivalent were directly applied to the evaluation of the modified Soderberg criterion, resulting in a very conservative design for structural optimization.

### 3.2. Fatigue damage analysis of lattice materials

To evaluate the fatigue damage of lattice materials, it is necessary to analyze both the effective material properties of the lattice structure and the equivalent mechanical response of the macroscale structure at the onset. The homogenization method has been widely employed to compute the effective material properties of lattices [73]. In this manner, the macroscopic effective elasticity tensor $D^H_{ijkl}$ of a lattice representative unit cell (RUC) can be determined as follows [74,75]:

$$D^H_{ijkl} = \frac{1}{|Y|}\int_Y \left(\varepsilon^{0(ij)}_{pq} - \varepsilon^{*(ij)}_{pq}\right) D_{pqrs}\left(\varepsilon^{0(kl)}_{rs} - \varepsilon^{*(kl)}_{rs}\right) dY \tag{20}$$

where $|Y|$ denotes the RUC volume and $\varepsilon^{0(kl)}_{rs}$ represents the prescribed macroscopic strain fields. The corresponding locally oscillating strain fields, denoted as $\varepsilon^{*(kl)}_{rs}$, are defined as follows:

$$\varepsilon^{*(kl)}_{rs} = \varepsilon_{rs}\left(u^{kl}\right) = \frac{1}{2}\left(u^{kl}_{r,s} + u^{kl}_{s,r}\right) \tag{21}$$

where $u^{kl}$ denotes the displacement field, which can be obtained by solving the following governing equation:

$$\int_Y D_{ijrs}\varepsilon_{ij}(v)\varepsilon_{rs}\left(u^{kl}\right) dY = \int_Y D_{ijrs}\varepsilon_{ij}(v)\varepsilon^{0(kl)}_{rs} dY, \forall v \in Y \tag{22}$$

where $v$ is a virtual displacement field. By virtue of the above homogenization method, the effective elasticity matrix $\boldsymbol{D}^H_e$ of the macroscale element $e$ can be determined.

Meanwhile, according to Eq. (8), the global stiffness matrix $\boldsymbol{K}$ incorporating lattice material properties can be reformulated as follows:

$$\boldsymbol{K} = \sum_{e=1}^{Ne} \int_{\overline{\Omega}_e} \boldsymbol{B}^{\mathrm{T}}_e \boldsymbol{D}^H_e \boldsymbol{B}_e |\boldsymbol{J}_1||\boldsymbol{J}_2| d\overline{\Omega} \tag{23}$$

Furthermore, from Eq. (9), the displacement and strain fields of the macroscale element can be obtained. Accordingly, the microscopic stress field $\sigma^{\mathrm{mi}}_{ij}$ within the RUC can be derived as:

$$\sigma^{\mathrm{mi}}_{ij} = D_{ijrs}\left(\varepsilon^{0(kl)}_{rs} - \varepsilon^{*(kl)}_{rs}\right)\varepsilon^{\mathrm{ma}(kl)} \tag{24}$$

where $\varepsilon^{\mathrm{ma}(kl)}$ is the macroscopic strain. The microscopic stress field of the lattice material can be reformulated as:

$$\begin{cases} \sigma^{\mathrm{mi}}_{ij} = \sigma'_{ijkl}\varepsilon^{\mathrm{ma}(kl)} \\ \sigma'_{ijkl} = D_{ijrs}\left(\varepsilon^{0(kl)}_{rs} - \varepsilon^{*(kl)}_{rs}\right) \end{cases} \tag{25}$$

where $\sigma'_{ijkl}$ represents the characteristic micro-scale stress field obtained under the influence of the imposed trial strain field $\varepsilon^0_{rs}$ in the RUC, while $\varepsilon^{\mathrm{mi}(kl)} = \varepsilon^{0(kl)}_{rs} - \varepsilon^{*(kl)}_{rs}$ represents the microscopic strain field.

The stress vector $\boldsymbol{\sigma}^{\mathrm{mi}}_{e,mie}$ of the *mie*-th microscopic subunit of the lattice material corresponding to the *e*-th macroscale element is expressed as:

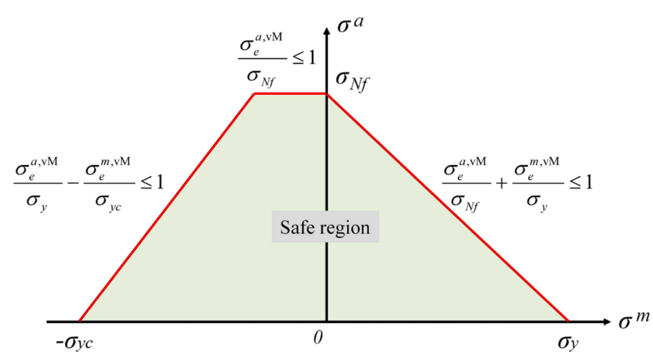


**Fig. 3.** Modified Soderberg fatigue diagram.

$$\boldsymbol{\sigma}_{e,mie}^{\mathrm{mi}} = \boldsymbol{D}_0 \boldsymbol{\varepsilon}_{e,mie}^{\mathrm{mi}} \boldsymbol{\varepsilon}_e^{\mathrm{ma}}, e = 1, 2, \ldots, Ne; mie = 1, 2, \ldots, Nmie \tag{26}$$

$$\boldsymbol{\sigma}_{e,mie}^{\mathrm{mi}} = \left[ \sigma'_{mie,xx} \varepsilon_{e,xx}^{\mathrm{ma}} \quad \sigma'_{mie,yy} \varepsilon_{e,yy}^{\mathrm{ma}} \quad \sigma'_{mie,xy} \varepsilon_{e,xy}^{\mathrm{ma}} \right]^{\mathrm{T}} \tag{27}$$

where $\boldsymbol{\varepsilon}_{e,mie}^{\mathrm{mi}}$ denotes the strain field of the *mie*-th microscale element, while $\boldsymbol{\varepsilon}_e^{\mathrm{ma}}$ represents the strain field of the *e*-th macroscale element, and $\varepsilon_{e,xx}^{\mathrm{ma}}$, $\varepsilon_{e,yy}^{\mathrm{ma}}$, $\varepsilon_{e,xy}^{\mathrm{ma}}$ denote the macroscale element strain components. *Nmie* is the total number of microscale elements into which each macroscale element is discretized.

In this study, the von Mises stress is employed to evaluate material failure at the microscale, expressed as:

$$\sigma_{e,mie}^{\mathrm{vMmi}} = \sqrt{\left(\boldsymbol{\sigma}_{e,mie}^{\mathrm{mi}}\right)^{\mathrm{T}} \boldsymbol{Q} \boldsymbol{\sigma}_{e,mie}^{\mathrm{mi}}} \tag{28}$$

The stress amplitude and mean stress vectors for the *mie*-th microscale element within the *e*-th macroscale element are defined as:

$$\begin{cases} \boldsymbol{\sigma}_{e,mie}^{\mathrm{mi},a} = c^a \boldsymbol{\sigma}_{e,mie}^{\mathrm{mi}} \\ \boldsymbol{\sigma}_{e,mie}^{\mathrm{mi},m} = c^m \boldsymbol{\sigma}_{e,mie}^{\mathrm{mi}} \end{cases} \tag{29}$$

The equivalent stress amplitude $\sigma_{e,mie}^{\mathrm{mi},a,\mathrm{vM}}$ and mean stress $\sigma_{e,mie}^{\mathrm{mi},m,\mathrm{vM}}$ for *mie*-th microscale element of the *e*-th macroscale element can thus be calculated as:

$$\begin{cases} \sigma_{e,mie}^{\mathrm{mi},a,\mathrm{vM}} = c^a \sqrt{\left(\boldsymbol{\sigma}_{e,mie}^{\mathrm{mi}}\right)^{\mathrm{T}} \boldsymbol{Q} \boldsymbol{\sigma}_{e,mie}^{\mathrm{mi}}} \\ \sigma_{e,mie}^{\mathrm{mi},m,\mathrm{vM}} = \mathrm{sign} \cdot c^m \sqrt{\left(\boldsymbol{\sigma}_{e,mie}^{\mathrm{mi}}\right)^{\mathrm{T}} \boldsymbol{Q} \boldsymbol{\sigma}_{e,mie}^{\mathrm{mi}}} \end{cases} \tag{30}$$

Therefore, the governing equation based on the modified Soderberg criterion for each microscale element within the macroscale element is given by:

$$D_{e,mie}^{SB} = \begin{cases} \dfrac{\sigma_{e,mie}^{\mathrm{mi},a,\mathrm{vM}}}{\sigma_{Nf}} + \dfrac{\sigma_{e,mie}^{\mathrm{mi},m,\mathrm{vM}}}{\sigma_y} \leq 1, \sigma_{e,mie}^{\mathrm{mi},m,\mathrm{vM}} \geq 0 \\ \dfrac{\sigma_{e,mie}^{\mathrm{mi},a,\mathrm{vM}}}{\sigma_y} - \dfrac{\sigma_{e,mie}^{\mathrm{mi},m,\mathrm{vM}}}{\sigma_{yc}} \leq 1, \sigma_{e,mie}^{\mathrm{mi},m,\mathrm{vM}} \leq \left(\dfrac{\sigma_{Nf}}{\sigma_y} - 1\right)\sigma_{yc} \\ \dfrac{\sigma_{e,mie}^{\mathrm{mi},a,\mathrm{vM}}}{\sigma_{Nf}} \leq 1, \left(\dfrac{\sigma_{Nf}}{\sigma_y} - 1\right)\sigma_{yc} < \sigma_{e,mie}^{\mathrm{mi},m,\mathrm{vM}} < 0 \end{cases} \tag{31}$$

### *3.3. Lattice materials with additive manufacturing-induced defects*

AM processes can introduce significant deviations between the designed geometry and the as-manufactured metallic lattice structures (see Fig. 4), which has a detrimental influence on desired mechanical and functional performance [16–18,64,76]. These geometric discrepancies are particularly pronounced along different printing directions, due to the inherent material deposition nonuniformity, an intrinsic anisotropic characteristic of lattice architecture [17,76].

According to the findings reported in [76], structures fabricated via SLM exhibit multiple kinds of manufacturing-induced deviations at the junctions, including parasitic masses, stepped features on diagonal struts, and thickness non-uniformity along the struts

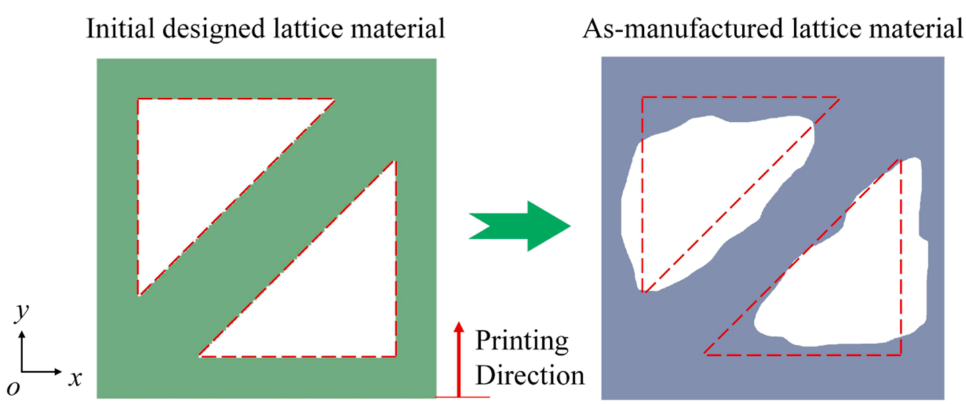


**Fig. 4.** Schematic comparison between the initial lattice design and the as-manufactured structure fabricated via selective laser melting.

(see Fig. 5). In particular, struts lying within the printing plane (0°) tend to suffer from excessive melting, resulting in manufactured dimensions that are larger than the intended design. As the printing angle increases, the extent of over-melting decreases, and the strut dimensions gradually shift. For struts oriented perpendicular to the printing plane (90°), the fabricated dimensions are generally smaller than the design specifications.

To reveal the influence of defects on the effective mechanical properties of lattices, several lattice concepts with intentional geometric defects were designed (Fig. 6), referring to the typical geometric deviations observed in AM processes and the experimental study of SLM-induced errors [76]. The geometric defects are explicitly governed by directional rules and bounding parameters with respect to the nominal strut thickness $t$. First, localized material accumulation predominantly occurs at horizontal struts and re-entrant joints, which is modeled with a maximum positive spatial deviation bound of up to $+\Delta t_{\max} = t$. Second, vertical or steeply inclined struts typically experience more severe under-melting, characterized by a negative spatial deviation down to $-\Delta t_{\min} = 0.5t$. Finally, structural boundaries within these defined envelopes are randomly perturbed to capture the realistic surface roughness. These explicit bounding parameters and phenomenological rules define the core generation logic of all defective microstructures evaluated herein. Subsequently, the effective mechanical properties of these imperfect lattice structures were evaluated using the homogenization method. Fig. 6 presents the lattice RUCs and their mechanical responses visualized through corresponding elastic curves.

Notably, in actual SLM 3D printing processes, geometric defects (such as surface roughness and local thickness variations) appear stochastically and are highly irregular. Therefore, the specific defective lattice configurations adopted in this study serve as representative benchmark models to rigorously verify the effectiveness and robustness of the proposed optimization method under severe geometric perturbations. In practical applications, realistic geometric defects (e.g., extracted from CT scans) can be directly implanted into the proposed framework to achieve fatigue-resistant optimization of lattice materials, accounting for actual manufacturing imperfections. Finally, to ensure strict reproducibility of the current numerical results, the exact geometric CAD models of these defective lattices are provided as supplementary files (refer to Appendix B).

## 4. MITO method considering fatigue damage of lattice materials

This section proposes an MITO method for constraining fatigue damage of lattice materials. The optimization objective is to minimize the compliance of the macrostructure, subject to two constraints: 1) limiting the fatigue damage within microscale elements, and 2) controlling the total material volume to remain within a specified fraction. The material distribution is optimized exclusively at the macroscale, while the geometric configuration of the lattice material is predetermined and remains invariant throughout the optimization process. Section 4.1 presents the complete mathematical formulation of the MITO problem considering fatigue damage of lattice materials. Section 4.2 introduces the material interpolation scheme based on the solid isotropic material with penalization (SIMP) method, along with the Heaviside projection technique to improve boundary clarity. Section 4.3 details the theoretical framework for implementing worst-case fatigue damage constraints, which effectively captures the potential maximum microscale fatigue damage of the lattice material during the optimization. In Section 4.4, the sensitivity analysis equations corresponding to the

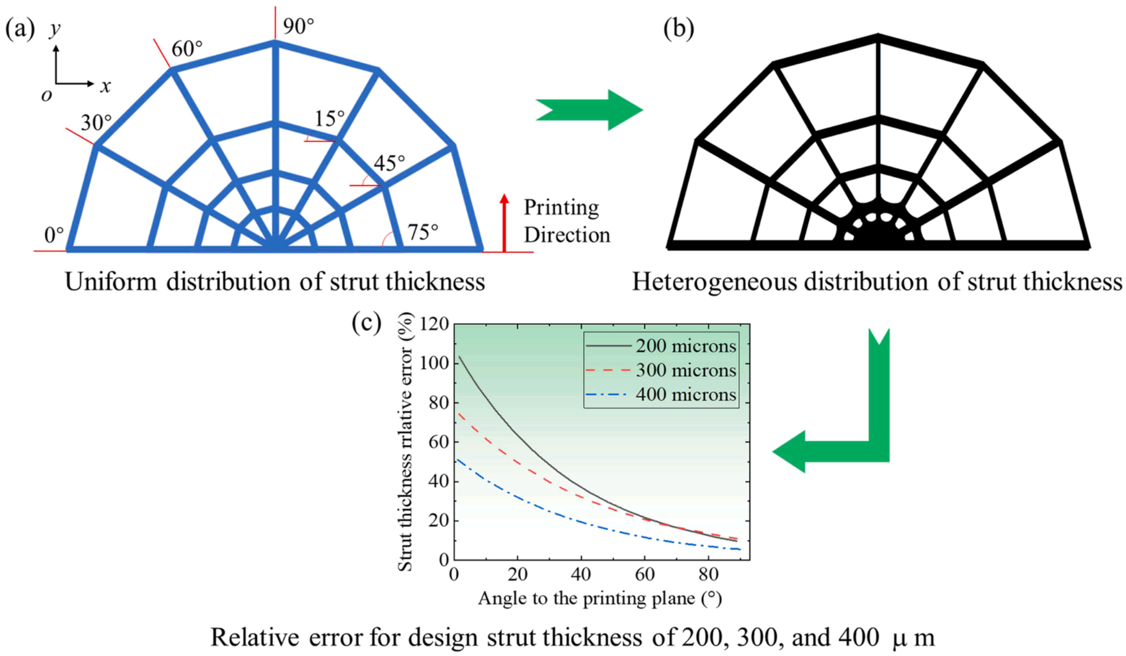


**Fig. 5.** Schematic of geometric deviation induced by SLM [76]: (a) schematic of the initial designed spider web, (b) schematic of the spider web fabricated by SLM, and (c) analysis of strut thickness errors (fitting curve).

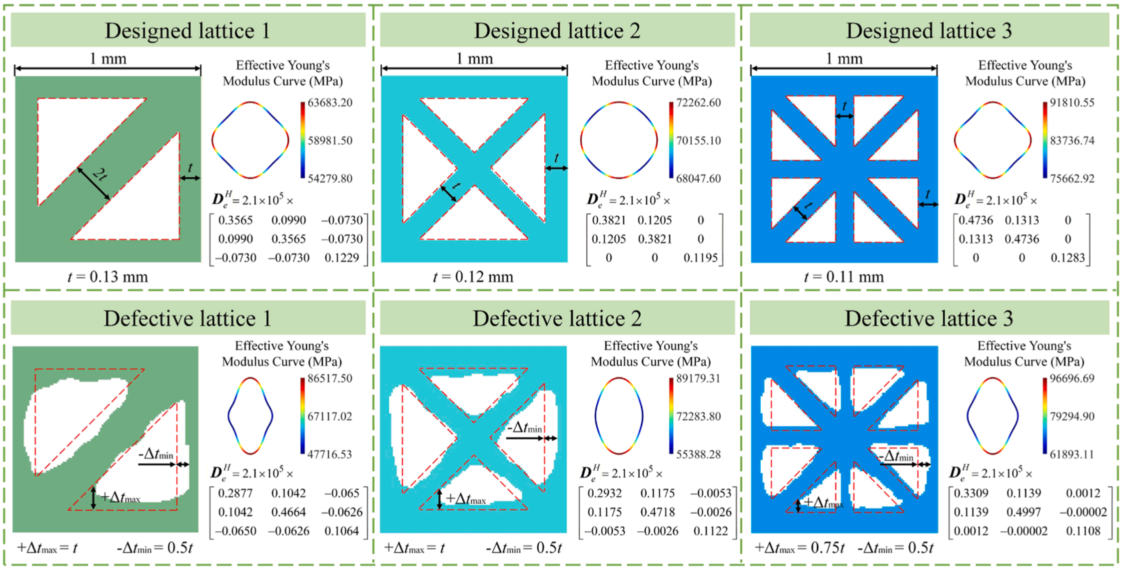


**Fig. 6.** Different lattice materials and their corresponding equivalent properties.

worst-case microscale fatigue damage constraints for lattice materials are derived, thereby providing a rigorous foundation for gradient-based optimization algorithms.

### 4.1. Optimization problem formulation

In this study, the relative density of each element is represented by the density value at its centroid, which is obtained through interpolation of the NURBS basis functions associated with the control points. The corresponding mathematical formulation of the MITO problem is expressed as follows:

$$\begin{aligned}
&\text{find}: \boldsymbol{\rho} \\
&\min: c(\boldsymbol{\rho}) = \boldsymbol{U}_1^{\mathrm{T}}\boldsymbol{K}\boldsymbol{U}_1 \\
&\text{s.t.}\begin{cases}
\boldsymbol{K}\boldsymbol{U}_1 = \boldsymbol{F}_{\max}, \boldsymbol{K}\boldsymbol{U}_2 = \boldsymbol{F}_{\min} \\
D_{e,mie}^{SB} \le 1 \\
V(\boldsymbol{\rho}) = \sum_{e=1}^{Ne} \rho_e v_e v^{\mathrm{mi}} \le VF \\
\rho_e = \sum_{i=1}^{n}\sum_{j=1}^{m} N_{i,p}^{j,q}(\xi_e,\eta_e)\widehat{\rho}_e^{i,j} \\
e = 1,2,\ldots,Ne; mie = 1,2,\ldots,Nmie \\
0 < \rho_{\min} \le \rho_e^{i,j} \le 1; i = 1,2,\ldots,n; j = 1,2,\ldots,m
\end{cases}
\end{aligned} \tag{32}$$

where $c(\boldsymbol{\rho})$ is the structural compliance, $\boldsymbol{U}_1$ denotes the global displacement vector resulting from the maximum load vector $\boldsymbol{F}_{\max}$, while $\boldsymbol{U}_2$ corresponds to the global displacement vector induced by the minimum load vector $\boldsymbol{F}_{\min}$, $V(\boldsymbol{\rho})$ denotes the overall structural volume, which accounts for the contributions from the embedded lattice material, $\rho_e$ and $v_e$ denote the relative density and volume of macro element $e$, respectively, $v^{\mathrm{mi}}$ is the volume of the unit cell structure, $VF$ is the prescribed total volume fraction, $\rho_e^{i,j}$ is the relative density of the control points of element $e$, $(\xi_e, \eta_e)$ denotes the coordinates in the parametric domain, $\widehat{\rho}_e^{i,j}$ represents the projected density associated with the control point, $\rho_{\min}$ is a small nonzero density assigned to void regions to ensure the numerical stability of the stiffness matrix during the optimization process, $n$ and $m$ are the number of control points in the $\xi$ and $\eta$ directions, respectively.

### 4.2. Material interpolation scheme and Heaviside projection

To optimize the spatial distribution of lattice materials on macroscopic scales, the MITO framework employs the SIMP method to define the relative density interpolation model [77]. The optimization focuses solely on the material layout at the macroscale, while the lattice configurations are predetermined to optimization. Each macroscale element is treated as a design variable associated with a corresponding macro-element. Accordingly, the interpolation of the effective elasticity matrix of the macrostructure, determined by the embedded lattice materials, is given by the following expression:

$$\boldsymbol{D}_e^{\mathrm{ma}} = (\rho_e)^{\varsigma} \boldsymbol{D}_e^H \tag{33}$$

where $\varsigma$ is a penalty factor, typically set to 3 to obtain a clear black-and-white solution.

By the implementation of the aforementioned material interpolation scheme, the interpolated element stiffness matrix $\boldsymbol{k}_e^{\mathrm{ma}}$ and the objective function $c(\boldsymbol{\rho})$ are expressed as follows:

$$\boldsymbol{k}_e^{\mathrm{ma}} = \int_{\overline{\Omega}_e} \boldsymbol{B}_e^{\mathrm{T}} \boldsymbol{D}_e^{\mathrm{ma}} \boldsymbol{B}_e |\boldsymbol{J}_1||\boldsymbol{J}_2| d\overline{\Omega} \tag{34}$$

$$c(\boldsymbol{\rho}) = \boldsymbol{U}_1^{\mathrm{T}} \boldsymbol{K} \boldsymbol{U}_1 = \sum_{e=1}^{Ne} (\boldsymbol{u}_e)_1^{\mathrm{T}} \boldsymbol{k}_e^{\mathrm{ma}} (\boldsymbol{u}_e)_1 \tag{35}$$

where $(\boldsymbol{u}_e)_1$ denotes the displacement vector of element $e$ induced by the maximum load vector $\boldsymbol{F}_{\max}$.

In this investigation, the Heaviside projection function is employed to project the control point densities, aiming to reduce the presence of gray elements in the optimized results [78]. The corresponding mathematical formulation is:

$$\widehat{\rho}_e^{i,j} = \frac{\tanh(\beta\alpha) + \tanh\left(\beta\left(\rho_e^{i,j} - \alpha\right)\right)}{\tanh(\beta\alpha) + \tanh(\beta(1-\alpha))} \tag{36}$$

where $\beta$ controls the curvature of the smoothed projection, while $\alpha$ is a threshold parameter that drives the density value toward either 0 or 1. In general, $\alpha$ is set to 0.5.

### 4.3. Fatigue damage constraints of lattice materials considering worst-case

In MITO, the design domain is discretized into a large number of NURBS elements, each corresponding to an RUC structure, consisting of a multitude of microscale elements. Imposing fatigue damage constraints on each microscale element will significantly increase the computational workload and may exceed the capabilities of gradient-based nonlinear optimization algorithms. To address this challenge, a worst-case analysis method is adopted to reduce the number of constraints [79,80]. Here, we only constrain the maximum fatigue damage observed among the microscale elements in each macroscale element. This strategy ensures the safety of the lattice material under extreme loading conditions while maintaining computational efficiency. Accordingly, the fatigue damage constraint for the most critical microscale element in macroscale element $e$ is defined as follows:

$$\max_{mie}\left(D_{e,mie}^{SB}\right) \le 1 \tag{37}$$

Derived from Eqs. (28)-(31), the above constraint can be reformulated as follows:

$$\max\left(D_{e,mie}^{SB}\right) = \begin{cases} \max\left(\dfrac{\sigma_{e,mie}^{\mathrm{mi},a,\mathrm{vM}}}{\sigma_{Nf}} + \dfrac{\sigma_{e,mie}^{\mathrm{mi},m,\mathrm{vM}}}{\sigma_y}\right) \le 1, \sigma_{e,mie}^{\mathrm{mi},m,\mathrm{vM}} \ge 0 \\ \max\left(\dfrac{\sigma_{e,mie}^{\mathrm{mi},a,\mathrm{vM}}}{\sigma_y} - \dfrac{\sigma_{e,mie}^{\mathrm{mi},m,\mathrm{vM}}}{\sigma_{yc}}\right) \le 1, \sigma_{e,mie}^{\mathrm{mi},m,\mathrm{vM}} \le \left(\dfrac{\sigma_{Nf}}{\sigma_y} - 1\right)\sigma_{yc} \\ \max\left(\dfrac{\sigma_{e,mie}^{\mathrm{mi},a,\mathrm{vM}}}{\sigma_{Nf}}\right) \le 1, \left(\dfrac{\sigma_{Nf}}{\sigma_y} - 1\right)\sigma_{yc} < \sigma_{e,mie}^{\mathrm{mi},m,\mathrm{vM}} < 0 \end{cases} \tag{38}$$

In the above derivations of Eqs. (28) and (30), the evaluation of the maximum fatigue damage within the lattice material is equivalent to determining the maximum microscale von Mises stress, $\max\left(\boldsymbol{\sigma}_{e,mie}^{\mathrm{vMmi}}\right)$. Therefore, to address the worst-case fatigue damage scenario, Eq. (26) can be reformulated as follows:

$$\begin{cases} \boldsymbol{\sigma}_{e,mie}^{\mathrm{mi}} = \boldsymbol{D}_0 \boldsymbol{\varepsilon}_{e,mie}^{\mathrm{mi}} \boldsymbol{\varepsilon}_e^{\mathrm{ma}} = \boldsymbol{D}_0 \boldsymbol{\varepsilon}_{e,mie}^{\mathrm{mi}} \left(\boldsymbol{D}_e^H\right)^{-1} \boldsymbol{\sigma}_e^{\mathrm{ma}} = \boldsymbol{D}_0 \boldsymbol{\varepsilon}_{e,mie}^{\mathrm{mi}} (\boldsymbol{D}_0)^{-1} \boldsymbol{\sigma}_e^{\mathrm{ma},0} \\ \boldsymbol{\sigma}_e^{\mathrm{ma}} = \boldsymbol{D}_e^H \boldsymbol{\varepsilon}_e^{\mathrm{ma}} \\ \boldsymbol{\sigma}_e^{\mathrm{ma},0} = \boldsymbol{D}_0 \boldsymbol{\varepsilon}_e^{\mathrm{ma}} \end{cases} \tag{39}$$

By introducing Eq. (39), Eq. (28) can be equivalently transformed into the following form:

$$\begin{cases} \sigma_{e,mie}^{\mathrm{vMmi}} = \sqrt{\left(\boldsymbol{\sigma}_e^{\mathrm{ma},0}\right)^{\mathrm{T}} \mathrm{M}_{mie} \boldsymbol{\sigma}_e^{\mathrm{ma},0}} \\ \mathrm{M}_{mie} = \left(\boldsymbol{D}_0 \boldsymbol{\varepsilon}_{e,mie}^{\mathrm{mi}} (\boldsymbol{D}_0)^{-1}\right)^{\mathrm{T}} \boldsymbol{Q} \boldsymbol{D}_0 \boldsymbol{\varepsilon}_{e,mie}^{\mathrm{mi}} (\boldsymbol{D}_0)^{-1} \end{cases} \tag{40}$$

The maximum von Mises stress among the microscale elements within the macroscale element $e$ is given by:

$$\max_{mie}\left(\sigma_{e,mie}^{\mathrm{vMmi}}\right)^2 = \max_{mie}\left(\vartheta_e^2\right) \tag{41}$$

where $\vartheta_e^2$ denotes the largest eigenvalue of matrix $\left(\boldsymbol{r}^{-1}\right)^{\mathrm{T}}\mathrm{M}_{mie}\boldsymbol{r}^{-1}$, and $\boldsymbol{r}^{\mathrm{T}}\boldsymbol{r} = \boldsymbol{Q}$.

Therefore, the maximum von Mises stress among the microscale elements within the $e$-th macroscale element can be computed as:

$$\max\left(\sigma_{e,mie}^{\mathrm{vMmi}}\right) : \overline{\sigma}_e^{\mathrm{vMmi}} = \vartheta_e\sqrt{\left(\boldsymbol{\sigma}_e^{\mathrm{ma},0}\right)^{\mathrm{T}}\boldsymbol{Q}\boldsymbol{\sigma}_e^{\mathrm{ma},0}} \tag{42}$$

where $\vartheta_e$ denotes the stress amplification factor for the $e$-th macroscale element, which is defined as the ratio of the maximum von Mises stress within the microscale elements to the von Mises stress of the corresponding macro element. The stress amplification factor reveals the influence of local stress concentrations at the microscale on the macrostructural response, playing a critical role in the fatigue-constrained MITO method.

Eventually, the fatigue damage constraint equation based on the modified Soderberg criterion, applied to the most critical (worst-case) microscale element within each macroscale element, is reformulated as follows:

$$\max\left(D_{e,mie}^{SB}\right) : \overline{D}_e^{SB} = \begin{cases} \dfrac{c^a\overline{\sigma}_e^{\mathrm{vMmi}}}{\sigma_{Nf}} + \dfrac{\mathrm{sign}\cdot c^m\overline{\sigma}_e^{\mathrm{vMmi}}}{\sigma_y} \le 1, \sigma_{e,mie}^{\mathrm{mi},m,\mathrm{vM}} \ge 0 \\ \dfrac{c^a\overline{\sigma}_e^{\mathrm{vMmi}}}{\sigma_y} - \dfrac{\mathrm{sign}\cdot c^m\overline{\sigma}_e^{\mathrm{vMmi}}}{\sigma_{yc}} \le 1, \sigma_{e,mie}^{\mathrm{mi},m,\mathrm{vM}} \le \left(\dfrac{\sigma_{Nf}}{\sigma_y} - 1\right)\sigma_{yc} \\ \dfrac{c^a\overline{\sigma}_e^{\mathrm{vMmi}}}{\sigma_{Nf}} \le 1, \left(\dfrac{\sigma_{Nf}}{\sigma_y} - 1\right)\sigma_{yc} < \sigma_{e,mie}^{\mathrm{mi},m,\mathrm{vM}} < 0 \end{cases} \tag{43}$$

This method ensures the lattice structure embedded within the macroscale element remains within safe fatigue limits under the most severe loading conditions.

Similar to stress constraints, fatigue damage constraints in topology optimization also involve a large number of conditions [38,81,82], making the explicit enforcement of each constraint computationally impractical. To alleviate heavy numerical computations caused by a large number of fatigue-related constraints, a $p$-norm aggregation function is employed as an approximation. The expression is defined as follows:

$$D_{pn}^{SB} = \left(\sum_{e=1}^{Ne}\left(\overline{D}_e^{SB}\right)^{\delta}\right)^{1/\delta} \le 1 \tag{44}$$

where $\delta$ is the $p$-norm coefficient.

To effectively apply local fatigue damage constraints, we adopt the modified $p$-norm method proposed by Le et al. [83] as an alternative to the conventional $p$-norm method. This enhanced technique incorporates scaling with respect to the results of previous optimization iterations, thereby achieving a more accurate approximation in maximum stress. In addition, it significantly mitigates numerical oscillations during the iterative process. The expression of the modified $p$-norm function is given as follows:

$$\begin{cases} \overline{D}_{pn}^{SB} \approx \chi^I D_{pn}^{SB} \le 1 \\ \chi^I = \varphi^I \dfrac{\max\left(\left(\overline{D}_e^{SB}\right)^{I-1}\right)}{\left(D_{pn}^{SB}\right)^{I-1}} + (1-\varphi^I)\chi^{I-1}, \varphi^I \in (0,1] \end{cases} \tag{45}$$

where $\chi^I$ represents the scaling factor in the $I$-th iteration, $\left(D_{pn}^{SB}\right)^{I-1}$ is the $p$-norm value of structural damage from the ($I$ - 1)-th iteration, and $\max\left(\left(\overline{D}_e^{SB}\right)^{I-1}\right)$ denotes the maximum structural damage value in the ($I$ - 1)-th iteration. If oscillations are detected during the optimization process, the parameter $\varphi^I$ is chosen between 0 and 1; otherwise, $\varphi^I$ is set to 1. As the number of optimization iterations increases, the fatigue damage constraint function gradually converges, resulting in $\left(D_{pn}^{SB}\right)^I \approx \left(D_{pn}^{SB}\right)^{I-1}$ and $\max\left(\left(\overline{D}_e^{SB}\right)^I\right) \approx \max\left(\left(\overline{D}_e^{SB}\right)^{I-1}\right)$. Eventually, the constraint function converges, satisfying $\chi^I D_{pn}^{SB} \approx \max\left(\left(\overline{D}_e^{SB}\right)^I\right)$. Further details on the modified $p$-norm method refer to [83,84].

Furthermore, the optimization of fatigue damage constraints encounters challenges similar to those in stress-constrained optimization, such as the occurrence of singular solutions and nonlinear behaviors. To address these issues, a relaxation method [85,86] is employed, which introduces a penalization of the stress term in Eq. (42). The relaxed stress is expressed as:

$$\overline{\boldsymbol{\sigma}}_e = \rho_e^{\gamma}\boldsymbol{\sigma}_e^{\mathrm{ma},0} = \rho_e^{\gamma}\boldsymbol{D}_0\boldsymbol{\varepsilon}_e^{\mathrm{ma}} = \rho_e^{\gamma}\boldsymbol{D}_0\boldsymbol{B}_e(\boldsymbol{u}_e)_1 \tag{46}$$

where $\gamma$ is the relaxation factor, which is typically set to 0.5.

### 4.4. Sensitivity analysis

In this study, a gradient-based optimization algorithm, specifically the Method of Moving Asymptotes (MMA) [87,88], is employed to solve the MITO problem that incorporates microscale fatigue damage constraints for lattice materials. The effectiveness of MMA is critically dependent on the accurate evaluation of sensitivities for both the objective and constraint functions with respect to the design variables. Since the sensitivity analysis of the compliance objective and the volume constraint has been extensively documented in previous literature, these derivations are not reiterated here. For completeness, the corresponding expressions are provided in Appendix A. Accordingly, this section focuses on deriving the sensitivity expression of the worst-case microscale fatigue damage constraint for lattice materials, which is formulated using the modified $p$-norm function. Based on the chain rule, the first-order sensitivity can be expressed as follows:

$$\frac{\partial \overline{D}_{pn}^{SB}}{\partial \rho_e^{i,j}} = \frac{\partial \overline{D}_{pn}^{SB}}{\partial D_{pn}^{SB}} \frac{\partial D_{pn}^{SB}}{\partial \overline{D}_e^{SB}} \frac{\partial \overline{D}_e^{SB}}{\partial \overline{\sigma}_e^{\mathrm{vMmi}}} \frac{\partial \overline{\sigma}_e^{\mathrm{vMmi}}}{\partial \overline{\boldsymbol{\sigma}}_e} \frac{\partial \overline{\boldsymbol{\sigma}}_e}{\partial \rho_e} \frac{\partial \rho_e}{\partial \widehat{\rho}_e^{i,j}} \frac{\partial \widehat{\rho}_e^{i,j}}{\partial \rho_e^{i,j}} \tag{47}$$

where the expressions $\frac{\partial \overline{D}_{pn}^{SB}}{\partial D_{pn}^{SB}}$ and $\frac{\partial D_{pn}^{SB}}{\partial \overline{D}_e^{SB}}$ are provided by Eq. (45):

$$\frac{\partial \overline{D}_{pn}^{SB}}{\partial D_{pn}^{SB}} = \chi^I \tag{48}$$

$$\frac{\partial D_{pn}^{SB}}{\partial \overline{D}_e^{SB}} = \left( \sum_{e=1}^{Ne} \left(\overline{D}_e^{SB}\right)^{\delta} \right)^{1/\delta - 1} \left(\overline{D}_e^{SB}\right)^{\delta - 1} \tag{49}$$

The term $\frac{\partial \overline{D}_e^{SB}}{\partial \overline{\sigma}_e^{\mathrm{vMmi}}}$ is defined according to Eq. (43), as follows:

$$\frac{\partial \overline{D}_e^{SB}}{\partial \overline{\sigma}_e^{\mathrm{vMmi}}} = \begin{cases} \dfrac{c^a}{\sigma_{Nf}} + \dfrac{\mathrm{sign} \cdot c^m}{\sigma_y}, \sigma_{e,mie}^{\mathrm{mi},m,\mathrm{vM}} \geq 0 \\ \dfrac{c^a}{\sigma_y} - \dfrac{\mathrm{sign} \cdot c^m}{\sigma_{yc}}, \sigma_{e,mie}^{\mathrm{mi},m,\mathrm{vM}} \leq \left( \dfrac{\sigma_{Nf}}{\sigma_y} - 1 \right) \sigma_{yc} \\ \dfrac{c^a}{\sigma_{Nf}}, \left( \dfrac{\sigma_{Nf}}{\sigma_y} - 1 \right) \sigma_{yc} < \sigma_{e,mie}^{\mathrm{mi},m,\mathrm{vM}} < 0 \end{cases} \tag{50}$$

According to Eq. (42), the expression for $\frac{\partial \overline{\sigma}_e^{\mathrm{vMmi}}}{\partial \overline{\boldsymbol{\sigma}}_e}$ is derived as:

$$\frac{\partial \overline{\sigma}_e^{\mathrm{vMmi}}}{\partial \overline{\boldsymbol{\sigma}}_e} = \vartheta_e \frac{1}{2\overline{\sigma}_e^{\mathrm{vMmi}}} \begin{Bmatrix} 2\sigma_{e,x}^{\mathrm{ma},0} - \sigma_{e,y}^{\mathrm{ma},0} \\ 2\sigma_{e,y}^{\mathrm{ma},0} - \sigma_{e,x}^{\mathrm{ma},0} \\ 6\sigma_{e,xy}^{\mathrm{ma},0} \end{Bmatrix} \tag{51}$$

Based on Eq. (46), the expression for $\frac{\partial \overline{\boldsymbol{\sigma}}_e}{\partial \rho_e}$ is given by:

$$\frac{\partial \overline{\boldsymbol{\sigma}}_e}{\partial \rho_e} = \gamma \rho_e^{\gamma - 1} \boldsymbol{D}_0 \boldsymbol{B}_e (\boldsymbol{u}_e)_1 + \rho_e^{\gamma} \boldsymbol{D}_0 \boldsymbol{B}_e \frac{\partial (\boldsymbol{u}_e)_1}{\partial \rho_e} \tag{52}$$

In this context, $\frac{\partial (\boldsymbol{u}_e)_1}{\partial \rho_e}$, which denotes the derivative of the displacement field with respect to the elemental density variable, is generally unknown. An adjoint method is employed to circumvent the direct computation of $\frac{\partial (\boldsymbol{u}_e)_1}{\partial \rho_e}$. According to Eqs. (6), (8), and (34), the corresponding adjoint equation can be formulated as:

$$\frac{\partial \boldsymbol{k}_e^{\mathrm{ma}}}{\partial \rho_e} (\boldsymbol{u}_e)_1 + \boldsymbol{k}_e^{\mathrm{ma}} \frac{\partial (\boldsymbol{u}_e)_1}{\partial \rho_e} = \boldsymbol{0} \tag{53}$$

where $\frac{\partial \boldsymbol{k}_e^{\mathrm{ma}}}{\partial \rho_e}$ is derived according to Eq. (34):

$$\frac{\partial \boldsymbol{k}_e^{\mathrm{ma}}}{\partial \rho_e} = \varsigma (\rho_e)^{\varsigma - 1} \int_{\overline{\Omega}_e} \boldsymbol{B}_e^{\mathrm{T}} \boldsymbol{D}_e^H \boldsymbol{B}_e |\boldsymbol{J}_1| |\boldsymbol{J}_2| d\overline{\Omega} \tag{54}$$

According to Eqs. (32) and (36), the expressions for quantities $\frac{\partial \rho_e}{\partial \widehat{\rho}_e^{i,j}}$ and $\frac{\partial \widehat{\rho}_e^{i,j}}{\partial \rho_e^{i,j}}$ are derived as:

$$\frac{\partial \rho_e}{\partial \widehat{\rho}_e^{i,j}} = \sum_{i=1}^{n} \sum_{j=1}^{m} \boldsymbol{N}_{i,p}^{j,q} (\xi_e, \eta_e) \tag{55}$$

$$\frac{\partial \hat{\rho}_e^{i,j}}{\partial \rho_e^{i,j}} = \frac{\beta\left(\operatorname{sech}\left(\beta\left(\rho_e^{i,j} - \alpha\right)\right)\right)^2}{\tanh(\beta\alpha) + \tanh(\beta(1-\alpha))} \tag{56}$$

To compute the unknown derivative term $\frac{\partial(\boldsymbol{u}_e)_1}{\partial \rho_e}$ in the governing equations, an adjoint vector is introduced, resulting in the following formulation:

$$\frac{\partial \overline{D}_{pn}^{SB}}{\partial \rho_e^{i,j}} = \boldsymbol{A}_e\left(\boldsymbol{C}_e\left(\gamma\rho_e^{\gamma-1}\boldsymbol{D}_0\boldsymbol{B}_e(\boldsymbol{u}_e)_1 + \rho_e^{\gamma}\boldsymbol{D}_0\boldsymbol{B}_e\frac{\partial(\boldsymbol{u}_e)_1}{\partial \rho_e}\right) + (\lambda_e)^{\mathrm{T}}\left(\boldsymbol{G}_e(\boldsymbol{u}_e)_1 + \boldsymbol{k}_e^{\mathrm{ma}}\frac{\partial(\boldsymbol{u}_e)_1}{\partial \rho_e}\right)\right)\boldsymbol{H}_e \tag{57}$$

where $\boldsymbol{A}_e$, $\boldsymbol{C}_e$, $\boldsymbol{G}_e$ and $\boldsymbol{H}_e$ are expressions as follows:

$$\boldsymbol{A}_e = \chi^I\left(\sum_{e=1}^{Ne}\left(\overline{D}_e^{SB}\right)^{\delta}\right)^{1/\delta-1}\left(\overline{D}_e^{SB}\right)^{\delta-1} \tag{58}$$

$$\boldsymbol{C}_e = \begin{cases} \left(\dfrac{c^a}{\sigma_{Nf}} + \dfrac{c^m}{\sigma_y}\right)\dfrac{\vartheta_e}{2\overline{\sigma}_e^{\mathrm{vMmi}}}\begin{Bmatrix} 2\sigma_{e,x}^{\mathrm{ma},0} - \sigma_{e,y}^{\mathrm{ma},0} \\ 2\sigma_{e,y}^{\mathrm{ma},0} - \sigma_{e,x}^{\mathrm{ma},0} \\ 6\sigma_{e,xy}^{\mathrm{ma},0} \end{Bmatrix}, \sigma_{e,mie}^{\mathrm{mi},m,\mathrm{vM}} \geq 0 \\ \left(\dfrac{c^a}{\sigma_y} - \dfrac{\mathrm{sign}\cdot c^m}{\sigma_{yc}}\right)\dfrac{\vartheta_e}{2\overline{\sigma}_e^{\mathrm{vMmi}}}\begin{Bmatrix} 2\sigma_{e,x}^{\mathrm{ma},0} - \sigma_{e,y}^{\mathrm{ma},0} \\ 2\sigma_{e,y}^{\mathrm{ma},0} - \sigma_{e,x}^{\mathrm{ma},0} \\ 6\sigma_{e,xy}^{\mathrm{ma},0} \end{Bmatrix}, \sigma_{e,mie}^{\mathrm{mi},m,\mathrm{vM}} \leq \left(\dfrac{\sigma_{Nf}}{\sigma_y} - 1\right)\sigma_{yc} \\ \left(\dfrac{c^a}{\sigma_{Nf}}\right)\dfrac{\vartheta_e}{2\overline{\sigma}_e^{\mathrm{vMmi}}}\begin{Bmatrix} 2\sigma_{e,x}^{\mathrm{ma},0} - \sigma_{e,y}^{\mathrm{ma},0} \\ 2\sigma_{e,y}^{\mathrm{ma},0} - \sigma_{e,x}^{\mathrm{ma},0} \\ 6\sigma_{e,xy}^{\mathrm{ma},0} \end{Bmatrix}, \left(\dfrac{\sigma_{Nf}}{\sigma_y} - 1\right)\sigma_{yc} < \sigma_{e,mie}^{\mathrm{mi},m,\mathrm{vM}} < 0 \end{cases} \tag{59}$$

$$\boldsymbol{G}_e = \varsigma(\rho_e)^{\varsigma-1}\int_{\Omega_e}\boldsymbol{B}_e^{\mathrm{T}}\boldsymbol{D}_e^{H}\boldsymbol{B}_e|\boldsymbol{J}_1||\boldsymbol{J}_2|d\overline{\Omega} \tag{60}$$

$$\boldsymbol{H}_e = \sum_{i=1}^{n}\sum_{j=1}^{m}\boldsymbol{N}_{i,p}^{j,q}(\xi_e,\eta_e)\frac{\beta\left(\operatorname{sech}\left(\beta\left(\rho_e^{i,j} - \alpha\right)\right)\right)^2}{\tanh(\beta\alpha) + \tanh(\beta(1-\alpha))} \tag{61}$$

Eq. (57) is reformulated accordingly as:

$$\frac{\partial \overline{D}_{pn}^{SB}}{\partial \rho_e^{i,j}} = \boldsymbol{A}_e\left(\boldsymbol{C}_e\gamma\rho_e^{\gamma-1}\boldsymbol{D}_0\boldsymbol{B}_e(\boldsymbol{u}_e)_1 + (\lambda_e)^{\mathrm{T}}\boldsymbol{G}_e(\boldsymbol{u}_e)_1 + \left(\boldsymbol{C}_e\rho_e^{\gamma}\boldsymbol{D}_0\boldsymbol{B}_e + (\lambda_e)^{\mathrm{T}}\boldsymbol{k}_e^{\mathrm{ma}}\right)\frac{\partial(\boldsymbol{u}_e)_1}{\partial \rho_e}\right)\boldsymbol{H}_e \tag{62}$$

In order to eliminate the unknown derivative term $\frac{\partial(\boldsymbol{u}_e)_1}{\partial \rho_e}$ in Eq. (62), the following procedure is adopted. Simultaneously, the adjoint vector $\boldsymbol{\lambda}_e$ is obtained.

$$\boldsymbol{C}_e\rho_e^{\gamma}\boldsymbol{D}_0\boldsymbol{B}_e + (\lambda_e)^{\mathrm{T}}\boldsymbol{k}_e^{\mathrm{ma}} = \boldsymbol{0} \tag{63}$$

$$\lambda_e = \left(-\boldsymbol{C}_e\rho_e^{\gamma}\boldsymbol{D}_0\boldsymbol{B}_e\left(\boldsymbol{k}_e^{\mathrm{ma}}\right)^{-1}\right)^{\mathrm{T}} \tag{64}$$

Eventually, the first-order sensitivity equation of the worst-case microscale fatigue damage constraint for lattice materials, based on the modified $p$-norm formulation, is derived as follows:

$$\frac{\partial \overline{D}_{pn}^{SB}}{\partial \rho_e^{i,j}} = \boldsymbol{A}_e\left(\left(\boldsymbol{C}_e\gamma\rho_e^{\gamma-1}\boldsymbol{D}_0\boldsymbol{B}_e(\boldsymbol{u}_e)_1 + (\lambda_e)^{\mathrm{T}}\boldsymbol{G}_e(\boldsymbol{u}_e)_1\right)\boldsymbol{H}_e \tag{65}$$

## 5. Numerical examples

In this section, several numerical examples are applied to demonstrate the effectiveness of the proposed MITO method that accounts for microscale fatigue damage of defective lattice materials. The overall implementation workflow is illustrated in Fig. 7. The convergence criterion is defined such that the change in the objective function is less than 0.001. In the numerical implementation, a steel is adopted as the base material, whose mechanical properties are listed in Table 1 [71]. The material is assumed to be isotropic and to exhibit linear elastic behavior throughout the analysis. The design domains for 2D and 3D structures are discretized using quadratic NURBS-based quadrilateral and hexahedral elements, respectively. The effective material properties of the macroscopic elements are evaluated via the homogenization method, employing a $100 \times 100$ microscale discretization for the 2D example and a $30 \times 30 \times 30$ microscale discretization for the 3D example. The initial density of each microscale element is set to 1.0, and the move limit in the MMA is specified as 0.02 to ensure stable convergence. Relevant optimization parameters used in the MITO framework are provided in Table 2. All examples are performed on a computer workstation equipped with an Intel® Core™ i7–13620H processor (2.4 GHz, 10 cores, 16 threads, 32 GB RAM), and the implementation is carried out in MATLAB® 2024b.

### 5.1. *Example 1: cantilever beam*

In the first example, a cantilever beam is employed to investigate the influence of geometric defects in lattice materials on the MITO results. Fig. 8 presents the design domain and boundary conditions of the beam. The left end of the beam is fully fixed, while a cyclic (fatigue) load is exerted at the central point of the right end cross-section along the negative $y$-axis with maximum and minimum loads of 38 N and 20 N, respectively. To explore the impact of different lattice configurations, three lattice concepts, as shown in Fig. 6 (including both as-designed and defective lattices), are adopted as the infill materials. The macro domain is discretized into 8192 elements, with a total volume fraction constraint of 0.3.

Fig. 9 presents the optimization results of the cantilever beam examples. The damage contours represent the maximum fatigue damage values within each micro-lattice unit cell. Fig. 10 illustrates the modified Soderberg diagrams associated with each instance, providing insight into the fatigue behavior under varying microstructural conditions. The convergence histories of the topology optimization for cantilever beams filled with designed and defective lattices are shown in Figs.11 and 12, respectively. A summary of the structural compliance, maximum von Mises stress, and maximum fatigue damage for each condition is provided in Table 3.

In this example, it is evident that variations in the underlying micro-lattice material significantly influence the resulting topology. As shown in Fig. 9(a), the optimized topology exhibits noticeable asymmetry, which is attributed to the intrinsic structural asymmetry of designed lattice 1, leading to material anisotropy. In contrast, Fig. 9(b) and (c) exhibit substantial symmetry in the optimized layouts, which is attributed to the geometrical symmetry of the designed Lattices 2 and 3. A clear distinction can also be observed when

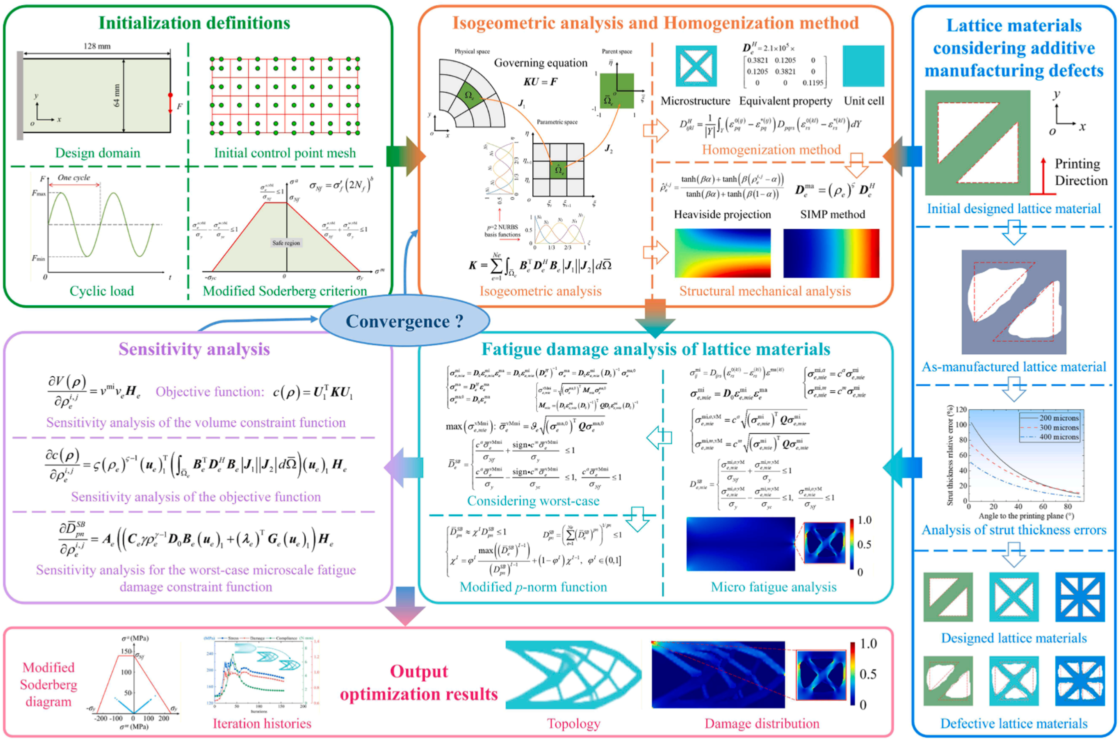


**Fig. 7.** Implementation flowchart of the proposed MITO method considering microscale fatigue damage of defective lattice materials.

**Table 1**
Material properties of a steel.

| Material property | Value |
|---|---|
| Young's modulus $E_0$ | 210 GPa |
| Poisson's ratio $\upsilon$ | 0.3 |
| Fatigue strength coefficient $\sigma'_f$ | 593 MPa |
| Fatigue strength exponent $b$ | −0.086 |
| The number of load reversals $N_f$ | $10^7$ |
| Yield tensile stress $\sigma_y$ | 240 MPa |
| Yield compressive stress $\sigma_{yc}$ | 240 MPa |
| Ultimate stress $\sigma_{ut}$ | 358 MPa |

**Table 2**
Optimization parameters for the proposed MITO method.

| Parameter | Value |
|---|---|
| Order of NURBS basis functions | 2 |
| Density penalty factor $\varsigma$ | 3 |
| $p$-norm coefficient $\delta$ | 12 |
| Stress relaxation factor $\gamma$ | 0.5 |
| Maximum iteration step | 300 |

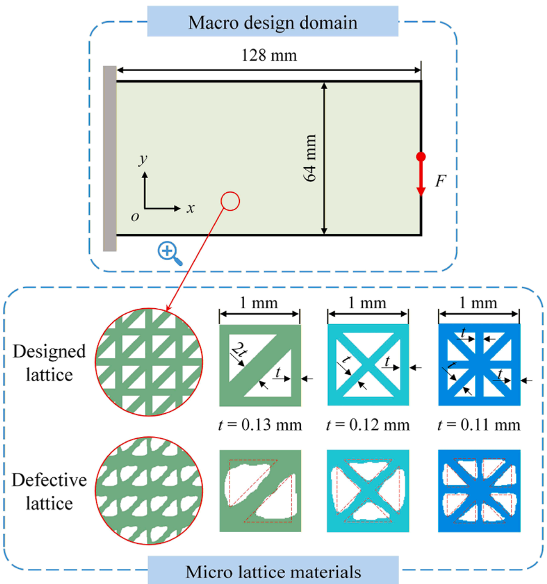


**Fig. 8.** Design domain and boundary conditions of the cantilever beam, along with different micro lattice materials.

comparing Fig. 9(d–f), which represent results obtained using defective lattices, with their designed counterparts in Fig. 9(a–c). Notably, the presence of geometric defects introduces substantial asymmetries in the topologies indicated in Fig. 9(e) and (f). From a structural mechanics perspective, the topological evolution observed in the defective lattice models represents an adaptive mechanism to counteract structural weakening. In the ideal model, the topology establishes direct and efficient load transfer paths. However, upon the introduction of manufacturing defects, both structural stiffness and load-bearing capacity are compromised. To compensate for this overall degradation, the optimization yields distinct topological configurations. Unlike the ideal case, which relies on minimal branching structures, the defective topology tends to retain auxiliary bracing struts. This introduces structural redundancy, ensuring that alternative load paths are available to prevent catastrophic failure in the event of local yielding caused by defects. These findings underscore the critical role that geometric defects in lattice materials contribute to altering the structural layout during the optimization process. It is therefore essential to account for such manufacturing-induced imperfections in topology optimization to ensure structural safety and load-bearing ability.

Furthermore, considering AM-induced defects in optimization results in a steep increase in compliance, with respective increases of 23.14%, 22.16%, and 23.89% compared to their designed lattice counterparts. Geometrical irregularities also lead to elevated maximum stress levels, with increases of 6.30%, 40.94%, and 68.97%, respectively. Consequently, the maximum fatigue damage

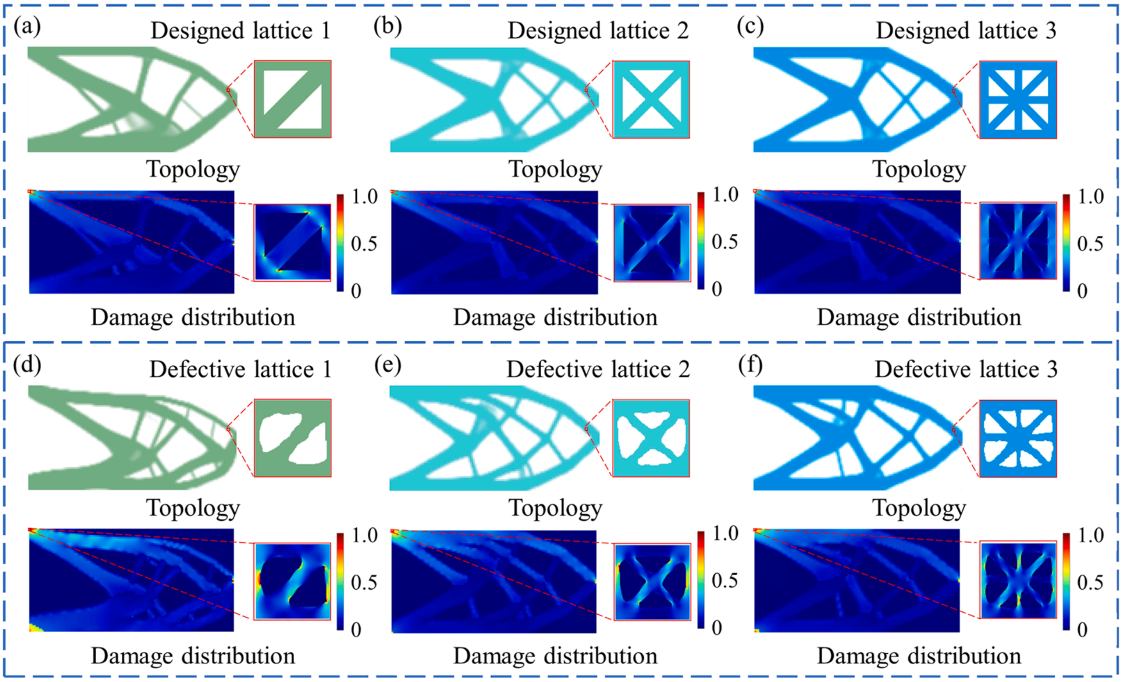


**Fig. 9.** Comparison of optimization results of the cantilever beam filled with designed and defective lattice materials: (a)-(c) designed lattices, and (d)-(f) defective lattices.

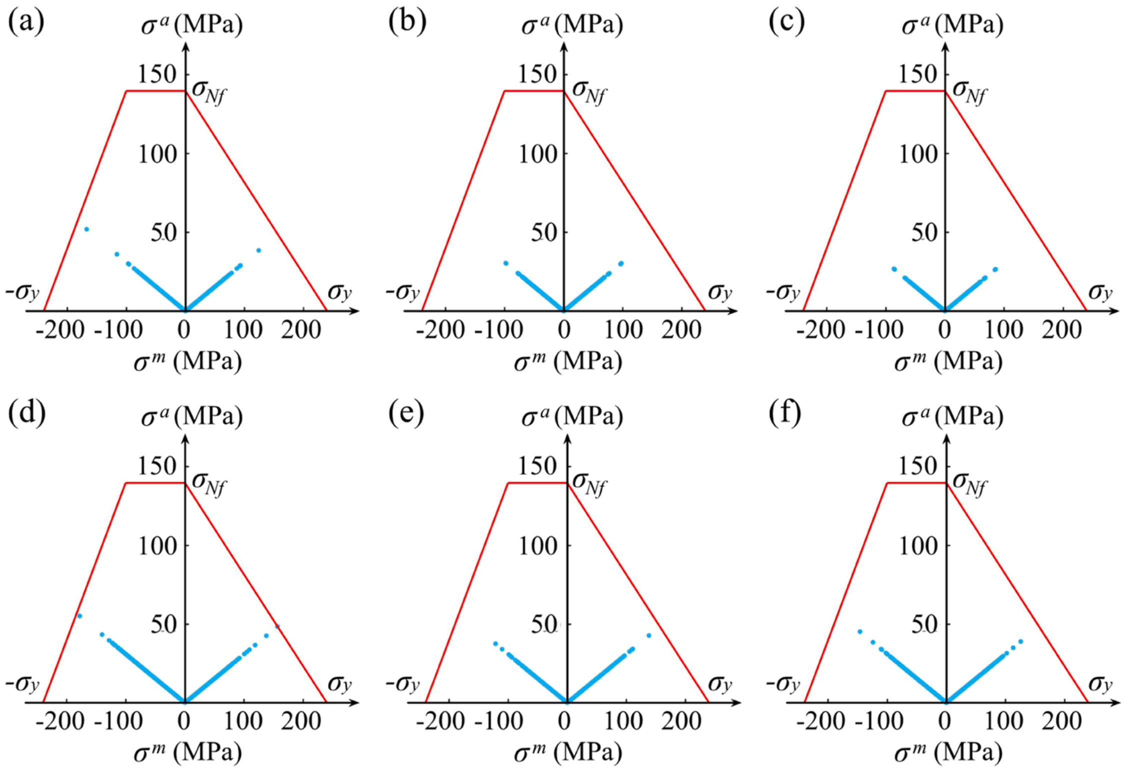


**Fig. 10.** Comparison of the modified Soderberg diagrams for the cantilever beam filled with designed and defective lattice materials: (a) designed lattice 1, (b) designed lattice 2, (c) designed lattice 3, (d) defective lattice 1, (e) defective lattice 2, and (f) defective lattice 3.

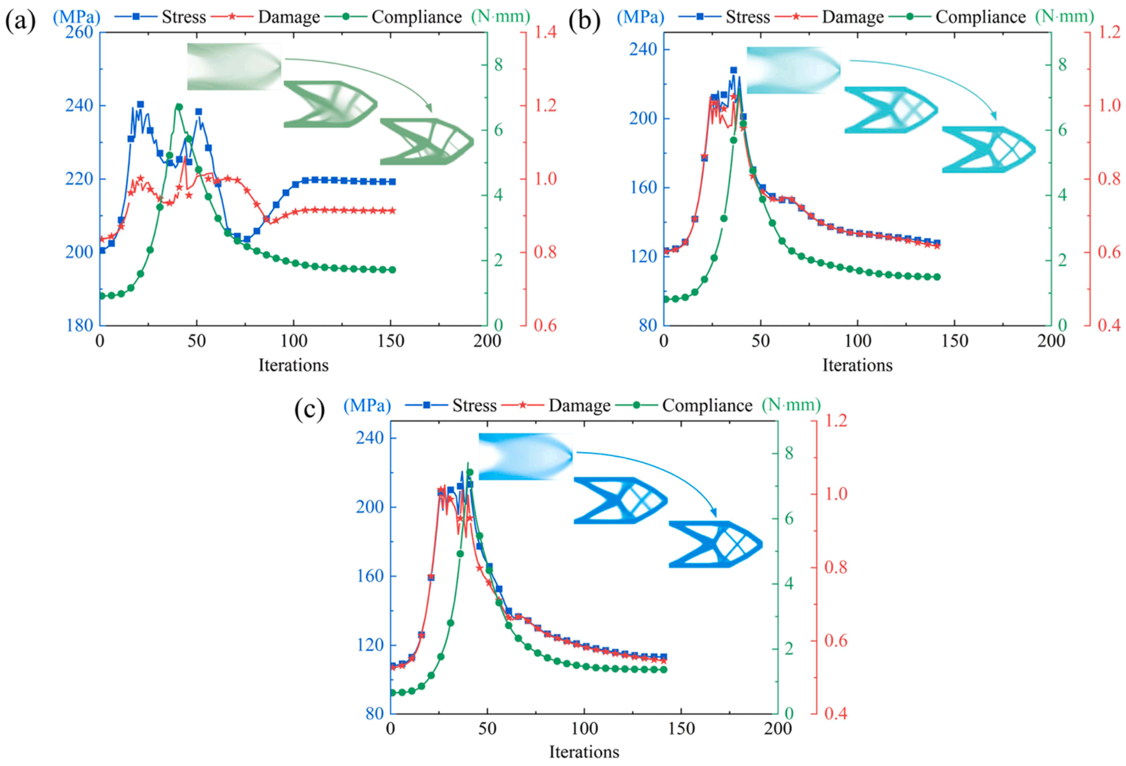


**Fig. 11.** Iteration histories of the cantilever beam filled with designed lattice materials: (a) designed lattice 1, (b) designed lattice 2, and (c) designed lattice 3.

values increase by 9.40%, 41.50%, and 47.07% for lattices 1, 2, and 3, respectively. These quantitative results highlight the detrimental effects of geometric imperfections on the fatigue performance of lattice-based structures. If ideal lattice designs are considered during fatigue-resistant optimization, the real AM-ed structure may suffer premature fatigue failure in service. Therefore, it is imperative to incorporate manufacturing-induced geometric defects into the structural design process to ensure accurate performance prediction and robust optimization.

It is worth noting that the selection of the $p$-norm coefficient $\delta$ is critical for balancing approximation accuracy and numerical stability. We therefore adopted distinct $p$-norm values $\delta \in \{4, 8, 12, 16, 20\}$ to analyze the fatigue damage aggregation behavior. By tracing the evolution of designed lattice 3 and defective lattice 3, we compared the aggregated $p$-norm values against the explicit maximum fatigue damage to identify the optimal parameter.

Figs.13 and 15 illustrate the final topological layouts for the designed and defective lattice 3, respectively. In the case of designed lattice materials, the optimized topologies remain topologically consistent for aggregation parameters $\delta \leq 12$. However, for $\delta > 12$, substantial topological deviations and symmetry breaking are observed. This behavior is attributed to the severe nonlinearity and numerical ill-conditioning induced by high $\delta$ values, which exacerbate the non-convexity of the problem and trap the optimizer in asymmetric local minima. In contrast, the defective lattice materials display a high sensitivity to $\delta$, with the topology evolving significantly as the parameter varies. This suggests that the complex stress fields induced by defects necessitate a more adaptive topological distribution. Moreover, the defective models consistently demonstrate inferior mechanical performance relative to the designed models. Specifically, at $\delta = 12$, the compliance deteriorates from 1.369 N·mm to 1.696 N·mm, and the maximum fatigue damage surges from 0.546 to 0.803. These findings quantitatively underscore the critical influence of manufacturing-induced geometric defects on degrading structural stiffness and fatigue durability.

To verify the accuracy of the aggregation function, Figs. 14 and 16 further compare the evolution of the $p$-norm approximation against the actual maximum fatigue damage throughout the optimization history for both lattice types. At $\delta = 4$, there is a significant deviation (gap) between the aggregated $p$-norm value and the actual maximum damage, indicating a large approximation error. As $\delta$ increases to 8 and 12, the $p$-norm curve rapidly approaches the maximum value curve. For $\delta > 12$ (e.g., $\delta = 16, 20$), the two curves almost completely overlap, implying that the $p$-norm effectively captures the maximum constraint behavior. Further increasing $\delta$ yields negligible accuracy gains (diminishing returns). Specifically for the lattice fatigue damage constraints considered in this study, the results confirm that $\delta = 12$ offers the optimal trade-off, ensuring high fidelity in damage approximation without inducing the numerical ill-conditioning characteristic of larger $\delta$ values.

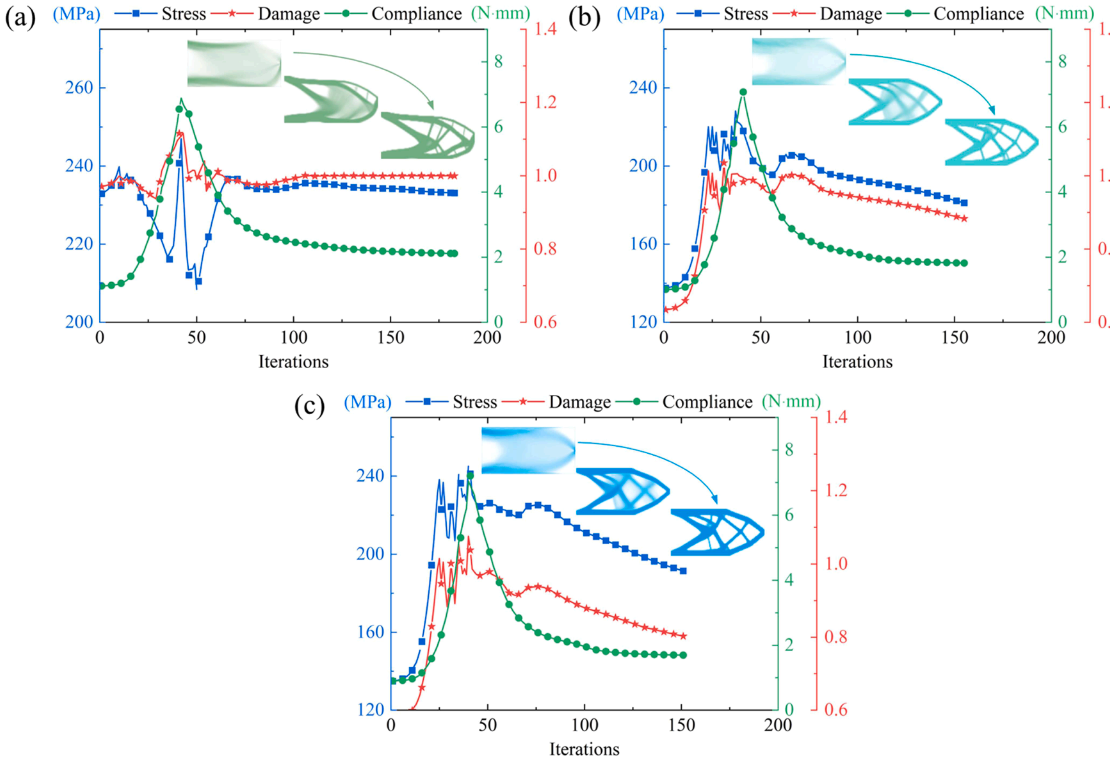


**Fig. 12.** Iteration histories of the cantilever beam filled with defective lattice materials: (a) defective lattice 1, (b) defective lattice 2, and (c) defective lattice 3.

**Table 3**
Comparison of compliance, maximum von Mises stress, and maximum fatigue damage of the cantilever beam filled with designed and defective lattice materials.

| Micro lattice | Lattice No. | Compliance (N·mm) | Max. stress (MPa) | Max. damage |
|---|---|---|---|---|
| Designed lattice | 1 | 1.716 | 219.269 | 0.914 |
| | 2 | 1.489 | 128.494 | 0.624 |
| | 3 | 1.369 | 113.306 | 0.546 |
| Defective lattice | 1 | 2.113 | 233.075 | 1.000 |
| | 2 | 1.819 | 181.102 | 0.883 |
| | 3 | 1.696 | 191.458 | 0.803 |

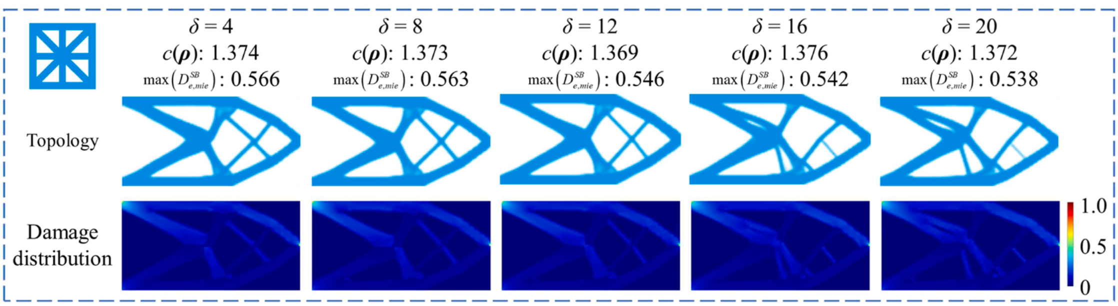


**Fig. 13.** Influence of the $p$-norm coefficient $\delta$ on the final topological layouts of the cantilever beam filled with the designed lattice 3.

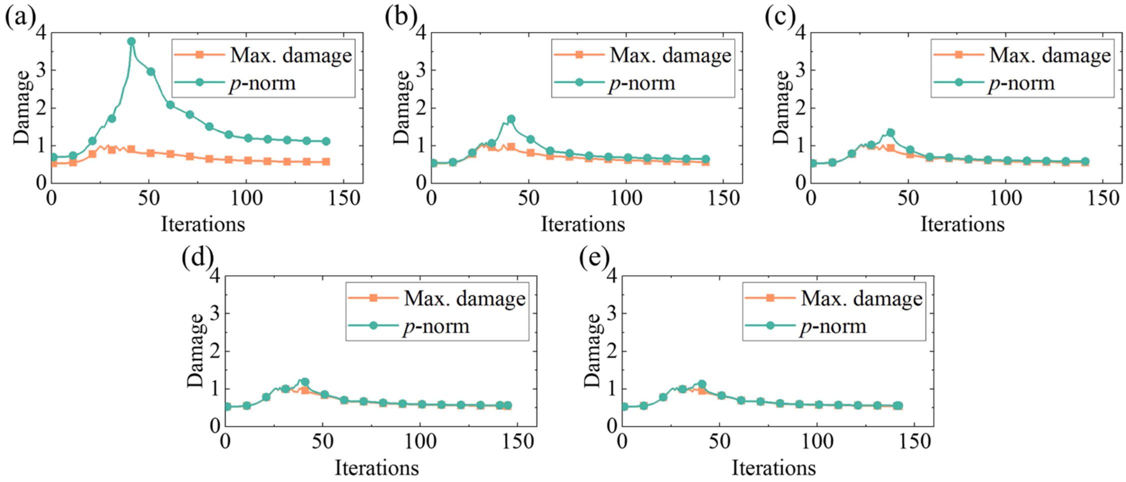


**Fig. 14.** Comparison of the $p$-norm approximation and the actual maximum fatigue damage throughout the optimization history for the cantilever beam filled with the designed lattice 3, under different aggregation parameters: (a) $\delta = 4$, (b) $\delta = 8$, (c) $\delta = 12$, (d) $\delta = 16$, and (e) $\delta = 20$.

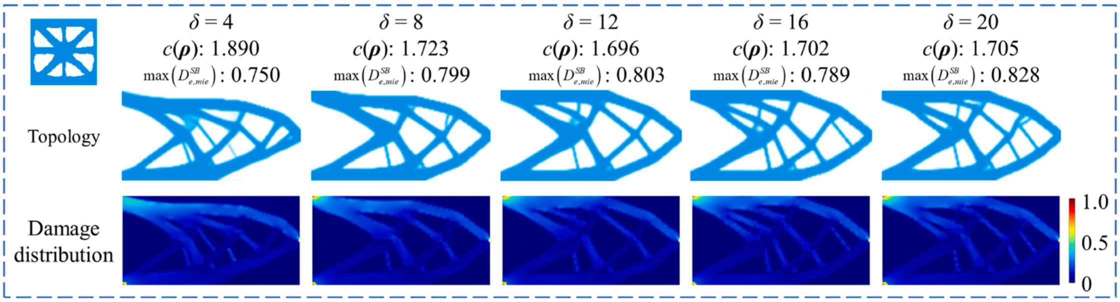


**Fig. 15.** Influence of the $p$-norm coefficient $\delta$ on the final topological layouts of the cantilever beam filled with the defective lattice 3.

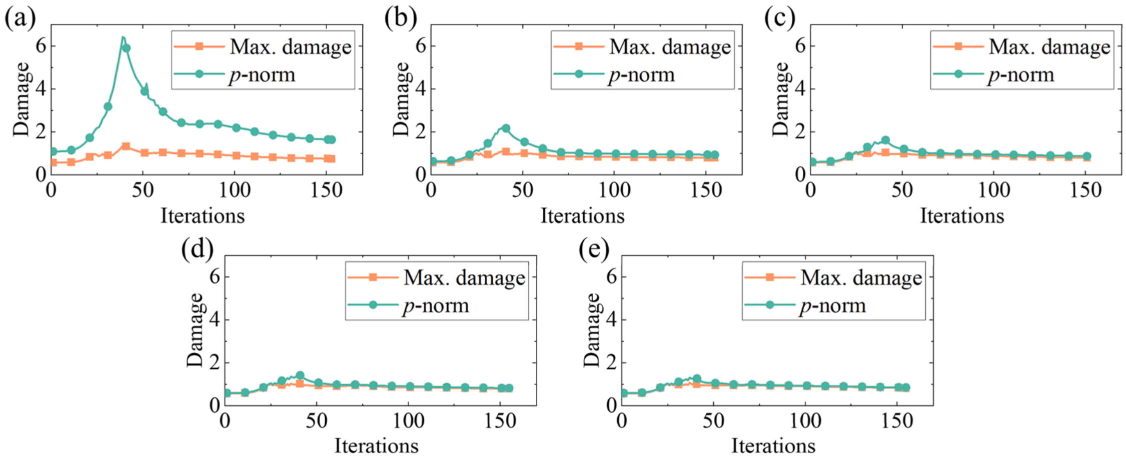


**Fig. 16.** Comparison of the $p$-norm approximation and the actual maximum fatigue damage throughout the optimization history for the cantilever beam filled with the defective lattice 3, under different aggregation parameters: (a) $\delta = 4$, (b) $\delta = 8$, (c) $\delta = 12$, (d) $\delta = 16$, and (e) $\delta = 20$.

### *5.2. Example 2:* L*-shaped beam*

To evaluate the effectiveness of the proposed MITO framework incorporating microscale fatigue damage for lattice materials, the classical L-shaped beam problem is employed as a benchmark. For comparison, a traditional stress-constrained optimization method is also implemented, with the maximum allowable stress set to a yield strength of $\sigma_y = 240\text{MPa}$. Fig. 17 illustrates the dimensions of the design domain and the applied boundary conditions. The applied external load is directed along the negative $y$-axis, with the maximum and minimum load magnitudes of 33 N and 6 N, respectively. In this example, three distinct microscale lattice configurations are employed as the infill material for the macrostructure. The macro domain is discretized using 10,608 elements, and the total volume fraction is limited to 0.2.

As shown in Fig. 18, varying the lattice structure type significantly alters the final optimized layout, even when the same optimization method is employed. The material distribution obtained by the fatigue-constrained method differs considerably from that of the stress-constrained method under identical micro lattice materials. Specifically, the fatigue-based method yields a smoother fillet at the corner of the L-shaped beam (Fig. 18(a–c)). This material layout is intended to alleviate stress concentrations, thereby avoiding excessive local stresses or damage in the micro lattice structure and satisfying fatigue constraints. In contrast, due to the relatively relaxed nature of stress constraints, the optimized structures obtained using the stress-constrained method exhibit less pronounced smoothing at the corner regions (see Fig. 18(d–f)). Additionally, the modified Soderberg criterion diagrams shown in Fig. 19 further illustrate this distinction. The structures optimized with fatigue constraints strictly maintain all stress states within the modified Soderberg safe domain. In contrast, the stress-constrained designs exhibit regions that violate the safety boundary, indicating a higher risk of fatigue failure during long-term service. These visual distinctions are quantitatively supported by the data summarized in Table 4. Compared to the stress-constrained method, the fatigue-constrained method significantly reduces the maximum stress in the structures by 18.26%, 32.28%, and 24.57% for the three defective lattice configurations, respectively. This improvement in fatigue performance comes at the expense of increased structural compliance, with corresponding increases of 9.08%, 17.10%, and 12.80%, respectively. Finally, the iteration histories (Figs. 20 and 21) confirm that both the fatigue-constrained and stress-constrained methods exhibit stable convergence behavior, successfully yielding these well-defined topologies.

Furthermore, the re-entrant corner of the L-shaped beam represents a typical stress concentration region where the force flow undergoes an abrupt change in direction. Both optimized designs exhibit curved features at the corner, guiding the stress flow strictly along the curvature to prevent stress concentration. Notably, compared to the stress-constrained design, the topology under fatigue constraints (Fig. 18(a–c)) evolves into a smoother and more rounded fillet. This further mitigates the detrimental effects of stress concentration. This geometric adaptation confirms that the proposed method goes beyond merely suppressing numerical peak stress values; it fundamentally optimizes the structural form to align with the principles of fracture mechanics.

In summary, under the same volume fraction constraint, the proposed method in this study yields structures with superior fatigue resistance compared to those obtained through conventional stress-based optimization method.

### 5.3. Example 3: simply supported structure

In the third example, the simply supported structure is employed to investigate the influence of different fatigue loading conditions on the optimization results. Fig. 22 displays the design domain and boundary conditions of the simply supported structure. In this example, defective lattices 2 and 3 are employed as the microscale infill materials for the simply supported structure. The cyclic (fatigue) load is applied at the midpoint of the bottom edge of the structure. Different load amplitudes are listed in Table 5. It is worth noting that in Case 1, the maximum and minimum load values are identical, representing a static loading scenario. The macro design domain is discretized using 8192 elements. During the optimization process, a total volume fraction constraint of 0.2 is imposed.

The results in Figs. 23–26, and Table 6 demonstrate that both loading conditions and micro defective lattice materials have a significant impact on the resulting optimized topology. For the same micro defective lattice, as the minimum load $\boldsymbol{F}_{\min}$ decreases, the overall fatigue damage within the structure increases. This trend is also reflected in Table 6, which reports an increase in maximum damage values. In the contour plots (see damage distribution in Figs. 23 and 25), this manifests as an expansion of high-damage regions

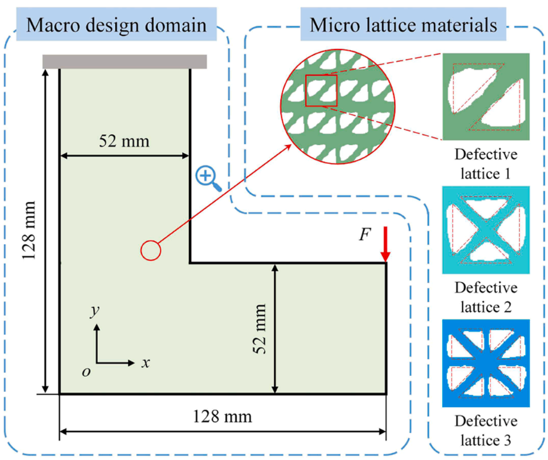


**Fig. 17.** Design domain and boundary conditions of the L-shaped beam, along with different defective lattice materials.

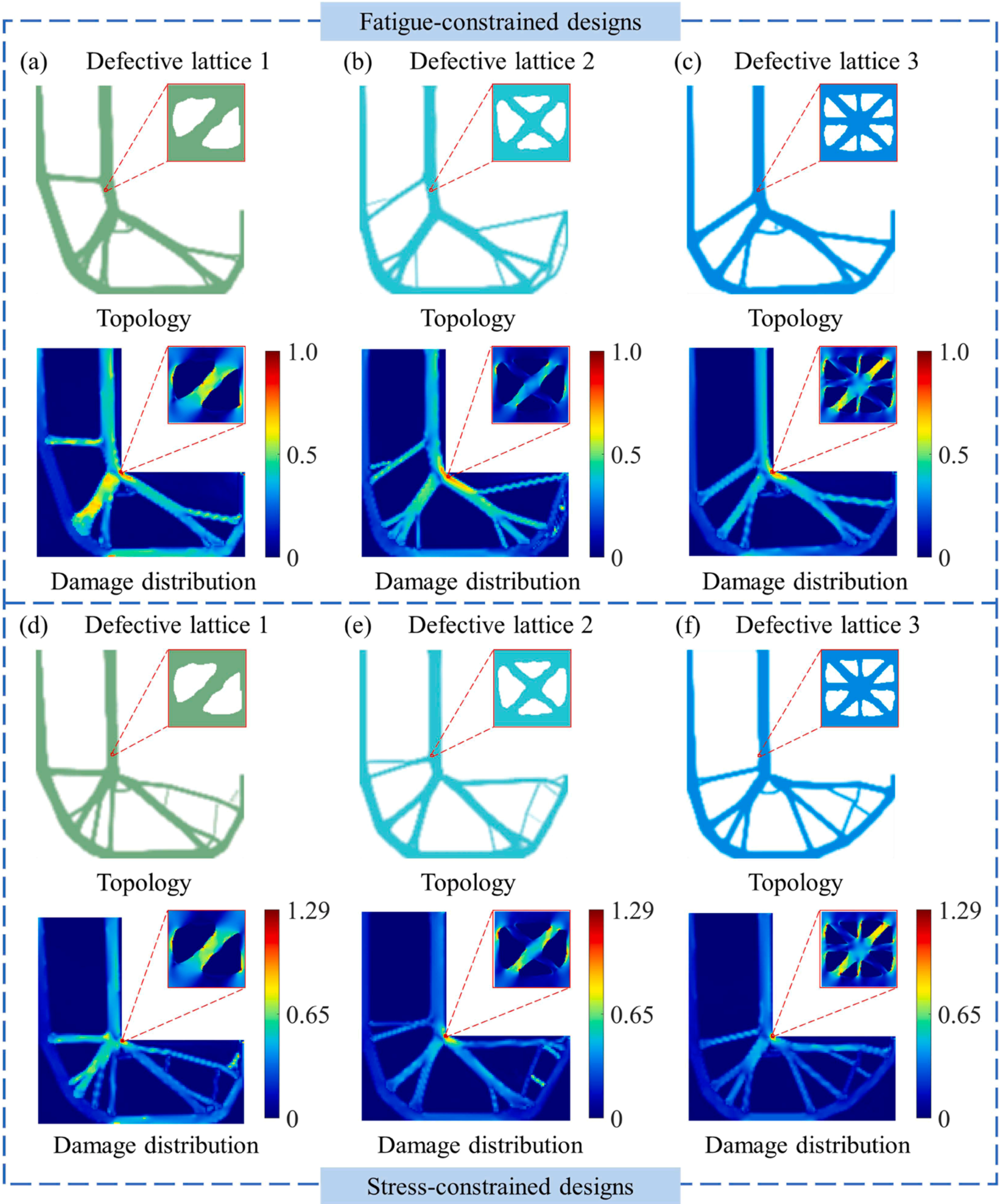


**Fig. 18.** Optimization results of the L-shaped beam with different methods and defective lattice materials: (a)-(c) fatigue constrained optimized results, and (d)-(f) stress constrained optimized results.

(i.e., larger colored areas and fewer blue zones), indicating that increased load amplitudes lead to greater fatigue-induced damage.

Meanwhile, Figs. 24 and 26 illustrate that the optimized structures successfully satisfy the fatigue constraints under various loading scenarios. As $\boldsymbol{F}_{\min}$ decreases, the points in the modified Soderberg diagrams shift progressively toward the vertical axis, which represents alternating stress. This observation highlights the increasing influence of alternating stress in fatigue-dominated structural design. Of particular note are Cases 1 and 5, which represent two extreme loading scenarios. In Case 1, where $\boldsymbol{F}_{\min} = \boldsymbol{F}_{\max}$, the structure is subject to purely static loading, and all points in the modified Soderberg diagram lie along the mean stress axis. In contrast, Case 5 corresponds to fully reversed loading, where $\boldsymbol{F}_{\min} = -\boldsymbol{F}_{\max}$, and the design points cluster around the amplitude stress axis.

These findings underscore the significant role of load amplitude in MITO with lattice material infill. When designing fatigue-

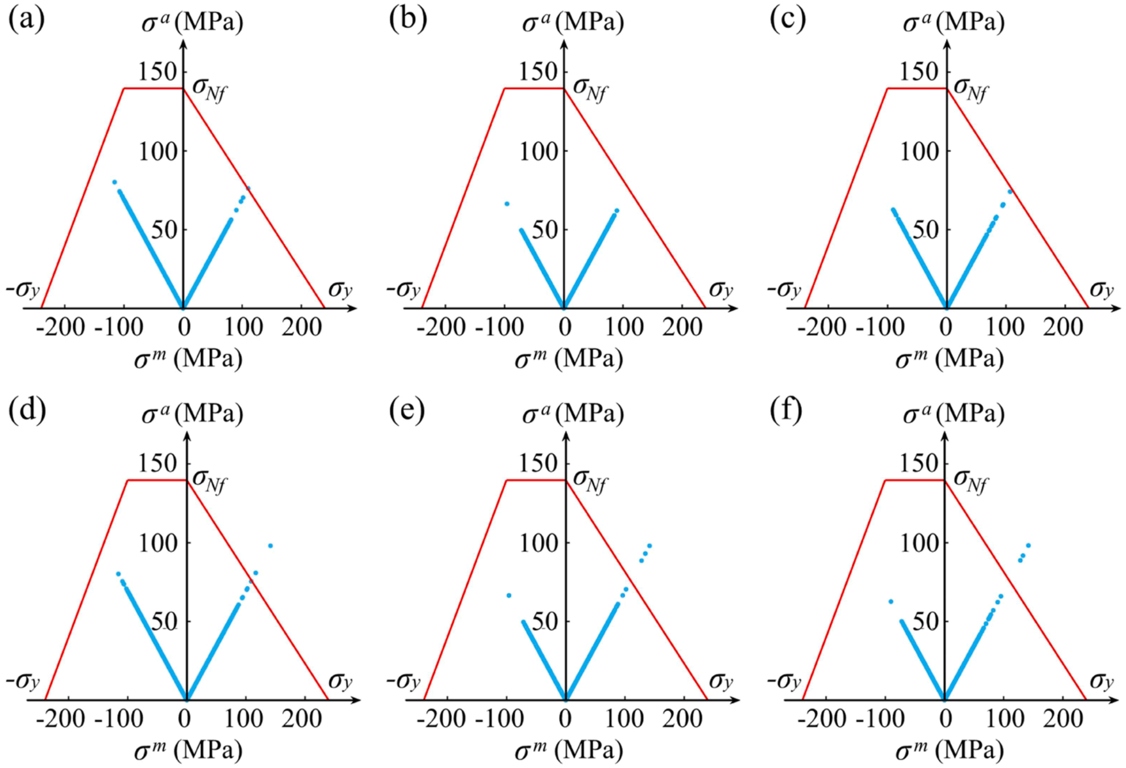


**Fig. 19.** Comparison of modified Soderberg diagrams for the L-shaped beam optimized with different methods and defective lattice materials: (a)-(c) fatigue-constrained designs; (d)-(f) stress-constrained designs; (a), (d) with defective lattice 1; (b), (e) with defective lattice 2; and (c), (f) with defective lattice 3.

**Table 4**
Comparison of compliance, maximum von Mises stress, and maximum fatigue damage of the L-shaped beam using different methods and defective lattice materials.

| Micro lattice | Method | Compliance (N·mm) | Max. stress (MPa) | Max. damage |
|---|---|---|---|---|
| Defective lattice 1 | Fatigue | 5.250 | 195.898 | 1.004 |
| | Stress | 4.813 | 239.672 | 1.292 |
| Defective lattice 2 | Fatigue | 5.313 | 162.255 | 0.791 |
| | Stress | 4.537 | 239.588 | 1.292 |
| Defective lattice 3 | Fatigue | 4.838 | 181.140 | 0.976 |
| | Stress | 4.289 | 240.140 | 1.295 |

resistant structures, it is crucial to account for the effects of varying load amplitudes on fatigue damage evolution to ensure robust and reliable performance over the service life.

### 5.4. Example 4: double L-shaped beam

To evaluate the applicability of the presented MITO method under different fatigue criteria, the modified Goodman criterion [34] is adopted in this section as an alternative fatigue constraint. The classical double L-shaped beam is selected as the benchmark problem, and its design domain, boundary conditions are illustrated in Fig. 27. Similarly, defective lattices 2 and 3 are used as the microscale infill materials for the double L-shaped beam. Identical loads are applied at both ends of the double L-shaped beam, acting in the negative $y$-direction, with a maximum load of 56 N and a minimum load of 16 N. The macro domain of the double L-shaped beam is discretized into 5304 elements. The total volume fraction constraint is set to 0.3 during the optimization process.

The fatigue diagram corresponding to the modified Goodman criterion is shown in Fig. 28. When the modified Goodman criterion is adopted as the fatigue constraint, the optimization problem presented in Section 4.1 can be reformulated as follows:

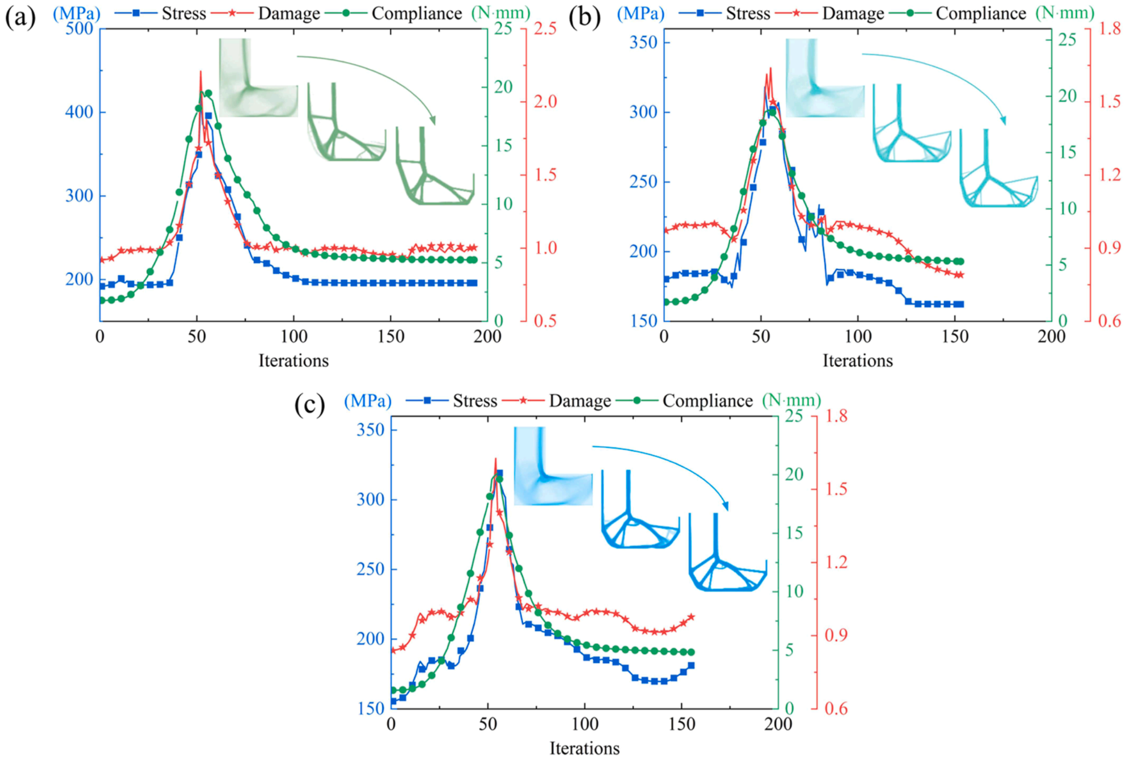


**Fig. 20.** Iteration histories of the L-shaped beam under the fatigue-constrained optimization: (a) defective lattice 1, (b) defective lattice 2, and (c) defective lattice 3.

$$
\begin{aligned}
&\text{find}: \boldsymbol{\rho}\\
&\min: c(\boldsymbol{\rho}) = \boldsymbol{U}_1^{\mathrm{T}}\boldsymbol{K}\boldsymbol{U}_1\\
&\text{s.t.}\begin{cases}
\boldsymbol{K}\boldsymbol{U}_1 = \boldsymbol{F}_{\max}, \boldsymbol{K}\boldsymbol{U}_2 = \boldsymbol{F}_{\min}\\
D_{e,mie}^{GD} \le 1\\
V(\boldsymbol{\rho}) = \sum_{e=1}^{Ne} \rho_e v_e v^{\mathrm{mi}} \le VF\\
\rho_e = \sum_{i=1}^{n}\sum_{j=1}^{m} N_{i,p}^{j,q}(\xi_e, \eta_e)\widehat{\rho}_e^{i,j}\\
e = 1, 2, \ldots, Ne; mie = 1, 2, \ldots, Nmie\\
0 < \rho_{\min} \le \rho_e^{i,j} \le 1; i = 1, 2, \ldots, n; j = 1, 2, \ldots, m
\end{cases}
\end{aligned}
\tag{66}
$$

where $D_{e,mie}^{GD}$ denotes the fatigue damage of the microscale element within the macroscale element, evaluated according to the Goodman criterion. Its expression is given as follows:

$$
D_{e,mie}^{GD} = \begin{cases}
\dfrac{\sigma_{e,mie}^{\mathrm{mi},a,\mathrm{vM}}}{\sigma_{Nf}} + \dfrac{\sigma_{e,mie}^{\mathrm{mi},m,\mathrm{vM}}}{\sigma_{ut}} \le 1, \sigma_{e,mie}^{\mathrm{mi},m,\mathrm{vM}} \ge 0\\[2ex]
\dfrac{\sigma_{e,mie}^{\mathrm{mi},a,\mathrm{vM}}}{\sigma_{y}} - \dfrac{\sigma_{e,mie}^{\mathrm{mi},m,\mathrm{vM}}}{\sigma_{yc}} \le 1, \sigma_{e,mie}^{\mathrm{mi},m,\mathrm{vM}} \le \left(\dfrac{\sigma_{Nf}}{\sigma_y} - 1\right)\sigma_{yc}\\[2ex]
\dfrac{\sigma_{e,mie}^{\mathrm{mi},a,\mathrm{vM}}}{\sigma_{Nf}} \le 1, \left(\dfrac{\sigma_{Nf}}{\sigma_y} - 1\right)\sigma_{yc} < \sigma_{e,mie}^{\mathrm{mi},m,\mathrm{vM}} < 0
\end{cases}
\tag{67}
$$

where $\sigma_{yc}$ represents the yield compressive stress of the material.

It is worth noting that the fatigue constraint formulation based on the modified Goodman criterion follows the same treatment as

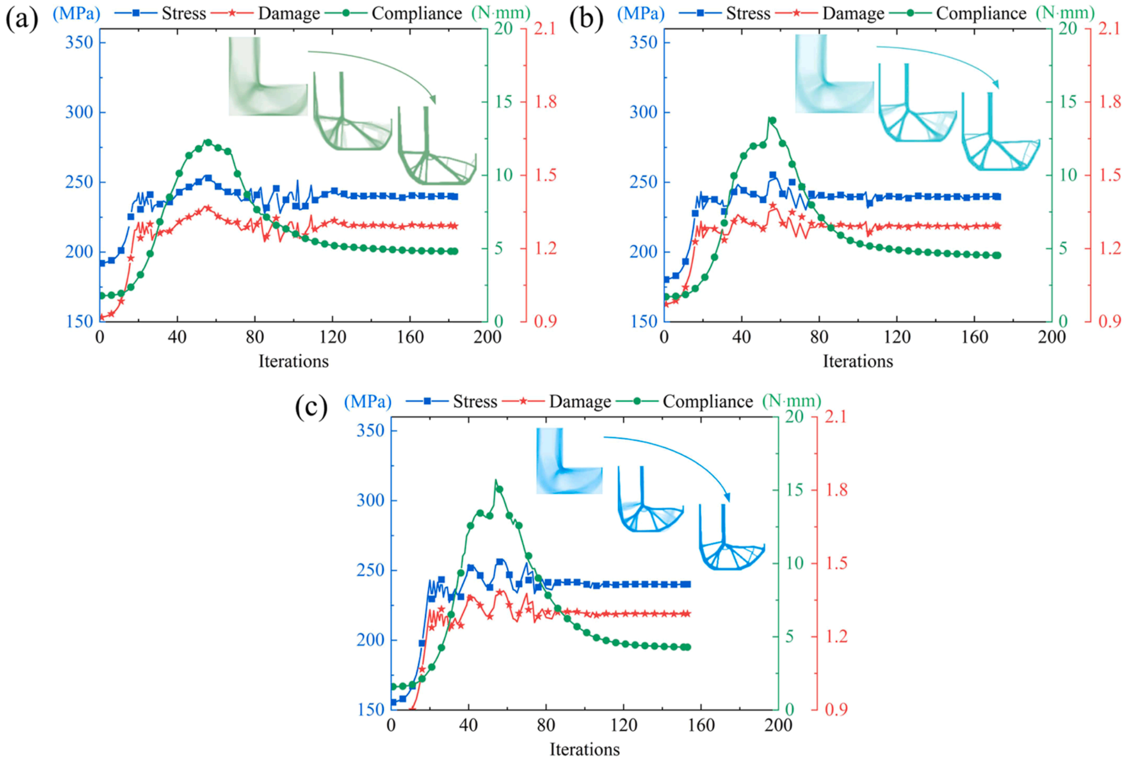


**Fig. 21.** Iteration histories of the L-shaped beam under the stress-constrained optimization: (a) defective lattice 1, (b) defective lattice 2, and (c) defective lattice 3.

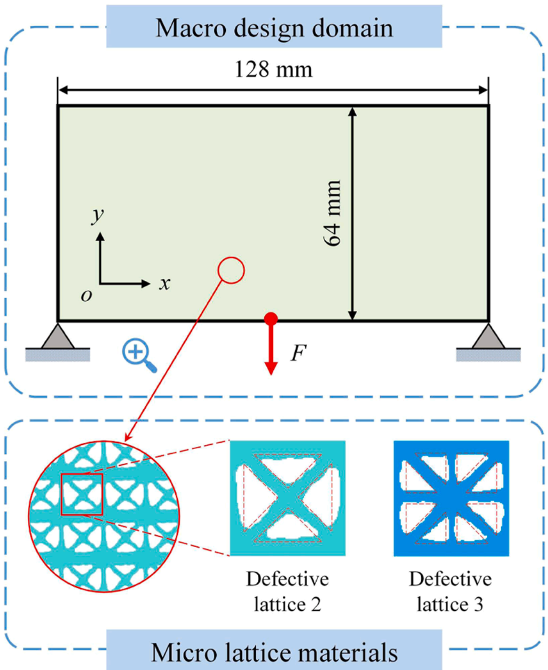


**Fig. 22.** Design domain and boundary conditions of the simply supported structure, along with different defective lattice materials.

**Table 5**
Different load amplitudes for the simply supported structure.

| Micro lattice | Case | Load amplitude (N) |
|---|---|---|
| Defective lattices 2 and 3 | 1 | $\boldsymbol{F}_{\max} = 60\text{N}, \boldsymbol{F}_{\min} = 60\text{N}$ |
| | 2 | $\boldsymbol{F}_{\max} = 60\text{N}, \boldsymbol{F}_{\min} = 30\text{N}$ |
| | 3 | $\boldsymbol{F}_{\max} = 60\text{N}, \boldsymbol{F}_{\min} = 0\text{N}$ |
| | 4 | $\boldsymbol{F}_{\max} = 60\text{N}, \boldsymbol{F}_{\min} = -30\text{N}$ |
| | 5 | $\boldsymbol{F}_{\max} = 60\text{N}, \boldsymbol{F}_{\min} = -60\text{N}$ |

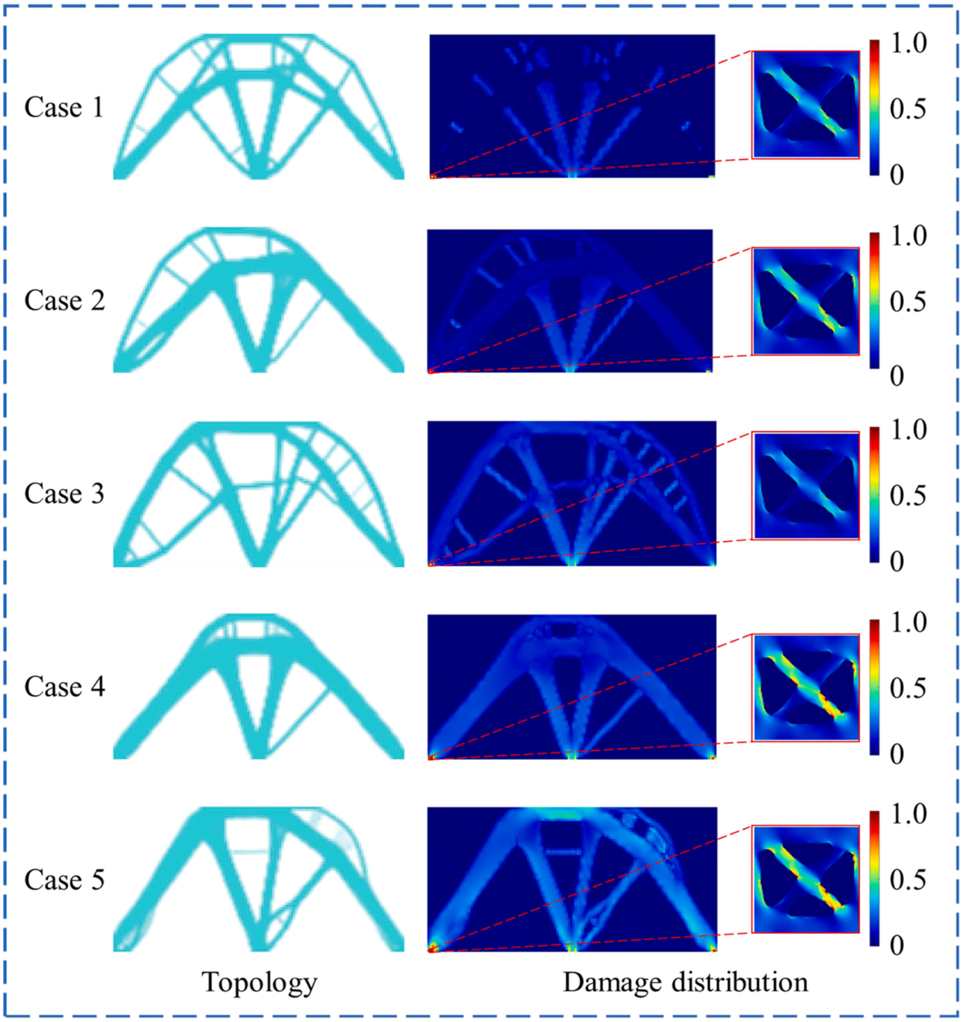


**Fig. 23.** Optimization results of the simply supported structure filled with the defective lattice 2.

that used for the modified Soderberg criterion. Since the sensitivity expression derived from the modified Goodman criterion is analogous to that of the modified Soderberg-based formulation, it is omitted here for brevity. Additionally, the parameter settings for both fatigue criteria remain consistent throughout the optimization process.

It is observed from Figs. 29–32 and Table 7 that both fatigue-constrained methods yield well-defined topological layouts, yet they exhibit distinct differences in both material distribution and overall mechanical performance. Specifically, the optimized structures based on the modified Soderberg criterion exhibit relatively higher values of fatigue damage, as indicated by the larger extent of colored (high-damage) regions and reduced low-damage (blue) zones. In contrast, the structures optimized under the Goodman criterion tend to show milder damage distributions. This distinction reflects the more conservative nature of the modified Soderberg criterion, which enforces stricter fatigue safety margins in the design process. Moreover, for the defective lattices 2 and 3, the structures optimized under the modified Goodman criterion exhibited a reduction in compliance by 0.54% and 3.87%, respectively, indicating an increase in overall stiffness. However, this stiffness enhancement was accompanied by an increase in maximum von

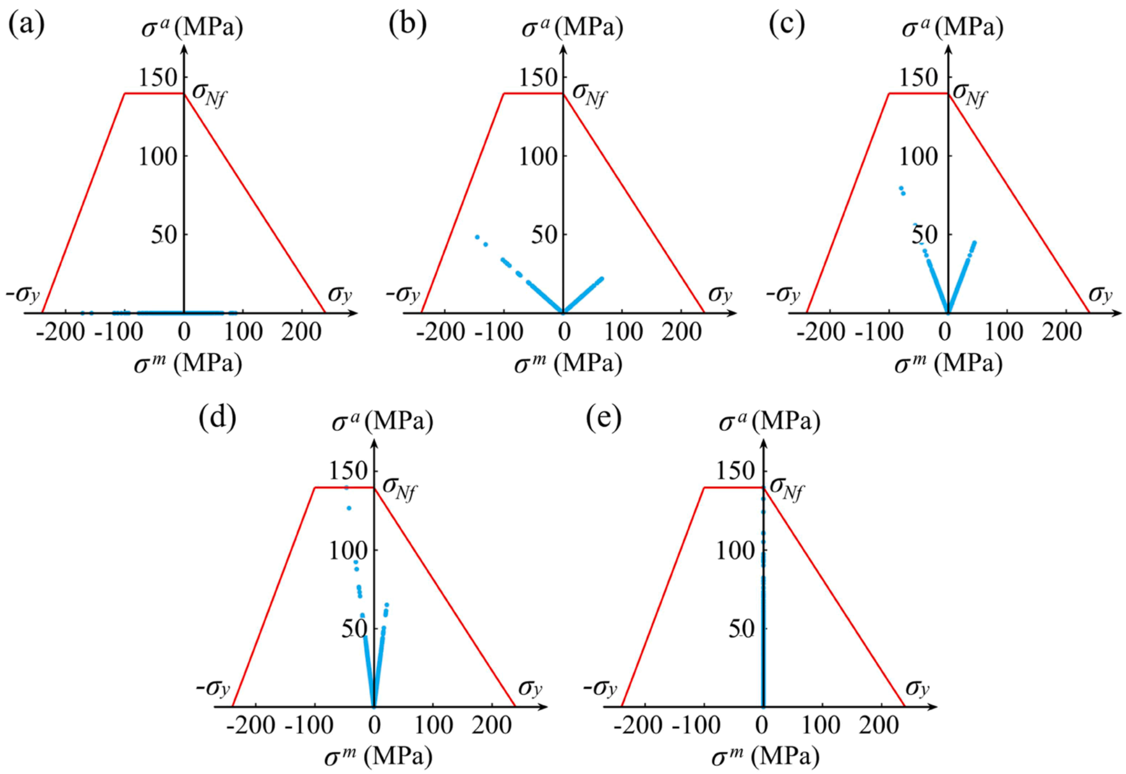


**Fig. 24.** Modified Soderberg diagrams of the simply supported structure filled with the defective lattice 2: (a) Case 1, (b) Case 2, (c) Case 3, (d) Case 4, and (e) Case 5.

Mises stress by 1.73% and 8.03%, respectively, which in turn compromised the fatigue resistance of the structures.

As shown in the fatigue damage diagrams (see Figs. 30 and 32), it can be seen that all design points (defined by the combination of mean stress and stress amplitude) remain strictly within the safe domain enclosed by the red boundary of the modified Soderberg diagram for structures optimized under the modified Soderberg criterion. For the Goodman-based designs, all stress points are contained within the corresponding safe domain defined by the blue Goodman boundary. However, some of these points may fall outside the modified Soderberg safe domain, highlighting that the Goodman criterion permits slightly higher fatigue risk in certain regions. This observation confirms that modified Soderberg-based optimization leads to more conservative designs compared to those based on the Goodman criterion, which is consistent with the mathematical formulation and graphical representation of the two criteria (see Figs. 3 and 28).

This example indicates that while both fatigue criteria can effectively guide the MITO process, they offer varying degrees of conservatism. The choice between them should therefore be informed by the safety requirements and fatigue sensitivity of the specific engineering application.

### 5.5. *Example 5: 3D cantilever beam*

In the fifth example, a 3D cantilever beam optimization problem is considered to assess the feasibility and effectiveness of the proposed MITO method in solving 3D structural optimization problems. The design domain, boundary conditions, and the employed 3D lattice materials are illustrated in Fig. 33. To comprehensively verify the feasibility of the proposed method for 3D problems, the 3D cantilever beam is optimized using three different lattice configurations: the 3D designed lattice, 3D defective lattice 1, and 3D defective lattice 2. The 3D cantilever beam is subjected to a maximum load of 42 N and a minimum load of 7 N, both applied in the negative $z$-direction. The macrostructure is discretized using 6250 elements. The total volume fraction constraint of 0.2 is limited. Additionally, the $p$-norm coefficient is set to $\delta = 8$. The rationale behind this parameter selection lies in the trade-off between approximation accuracy and convergence behavior. In 3D scenarios, stronger nonlinearities necessitate a smaller $\delta$ to ensure stable convergence.

Fig. 34(a–c) illustrate the optimized macroscale topological layouts. The observed topologies derived from the designed lattice and the two defect lattice models exhibit differences. To compensate for the degraded stiffness and load-bearing capacity of the defective microstructures, the optimizer autonomously redistributes the material, noticeably thickening the primary load-bearing members (e.g., the lower curved boundaries in Fig. 34(b) and (c)) and creating more robust 3D load transfer paths.

The effectiveness of the fatigue constraint is validated through the damage distributions (Fig. 34(d–f)) and the corresponding

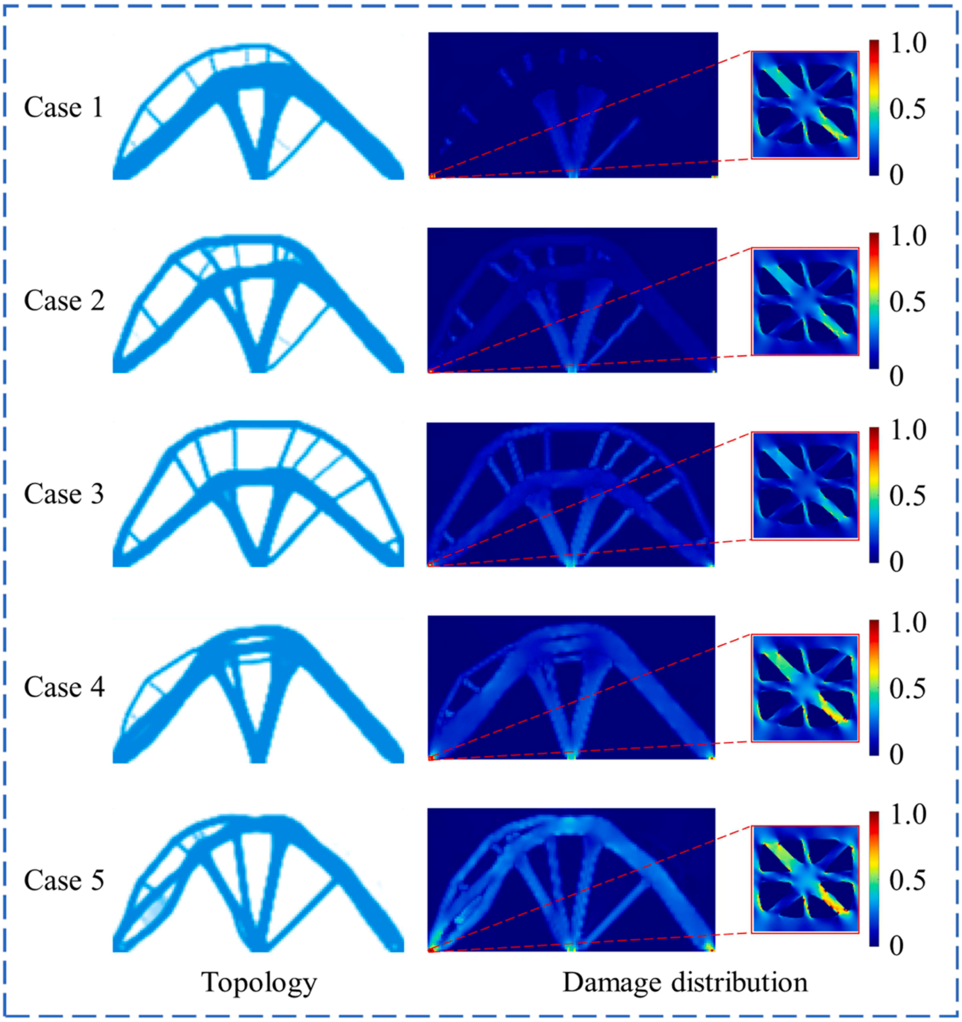


**Fig. 25.** Optimization results of the simply supported structure filled with the defective lattice 3.

modified Soderberg diagrams (Fig. 34(g–i)). Despite the severe stress concentrations inherently caused by the microscale defects, the maximum fatigue damage in all three scenarios is strictly controlled below the critical threshold of 1.0. These results confirm the feasibility and robustness of the proposed method for fatigue-resistant design of 3D defective lattice structures.

The results are further corroborated by the quantitative comparisons summarized in Table 8. The introduction of microscale defects inevitably deteriorates the overall structural performance. Compared to the ideal design (Compliance = 0.600 N·mm), the structures filled with defective lattice 1 and defective lattice 2 exhibit higher compliances of 0.723 N·mm and 0.741 N·mm, respectively. Similarly, the maximum microscale fatigue damage escalates from 0.621 in the ideal model to 0.912 and 0.864 in the defective models. These metrics quantitatively underscore the detrimental impact of manufacturing defects on macroscopic stiffness and durability, highlighting the critical necessity of integrating explicit defect models into the multiscale optimization loop to ensure genuine structural safety.

## 6. Conclusions

In this work, an MITO method considering microscale fatigue damage constraints of defective lattice materials is presented. An IGA-based computational procedure was established for evaluating the microscale fatigue damage of lattices. Afterwards, an MITO model incorporating fatigue damage constraints is formulated. The cantilever beam example highlights the critical importance of incorporating lattice defects into the optimization framework. The optimized structures derived from defective lattices show notably inferior fatigue performance compared to those based on damage-free lattice configurations. The effectiveness of the proposed method is demonstrated through an L-shaped beam example, which shows superior fatigue resistance compared to traditional stress-constrained optimization. The influence of different fatigue loading amplitudes is further investigated using the simply supported structure filled with different defective lattice materials. Moreover, the developed framework is extended to incorporate the modified

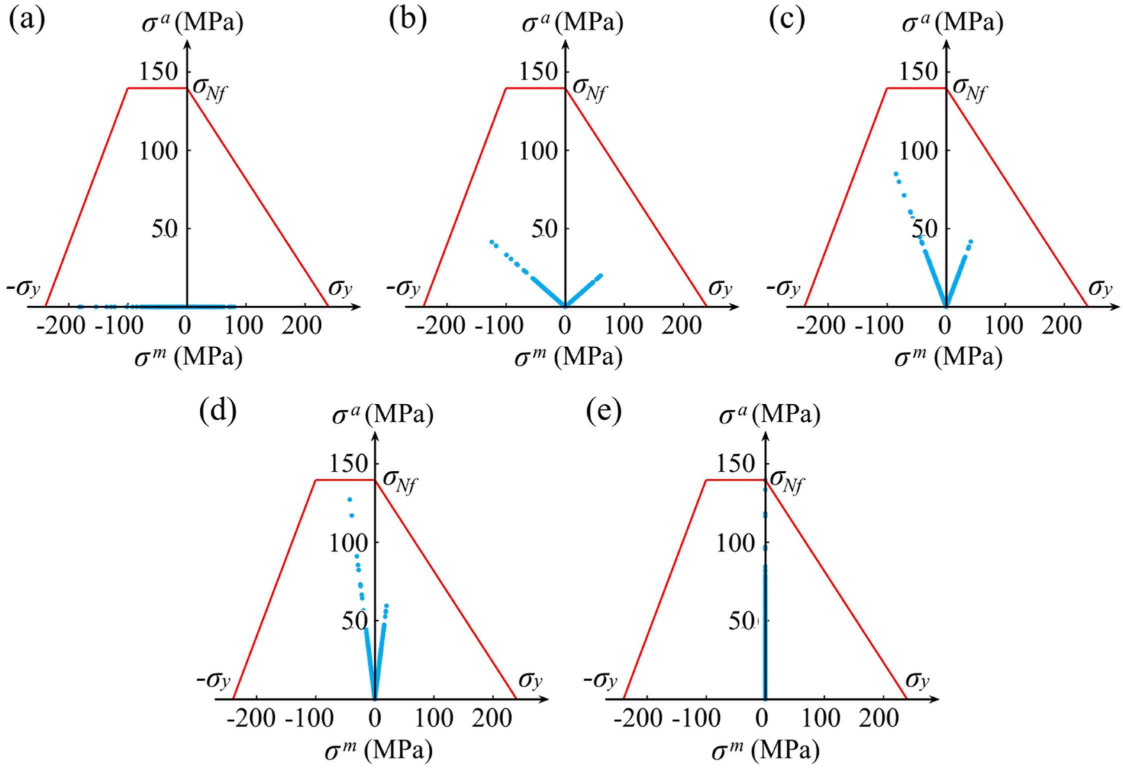


**Fig. 26.** Modified Soderberg diagrams of the simply supported structure filled with the defective lattice 3: (a) Case 1, (b) Case 2, (c) Case 3, (d) Case 4, and (e) Case 5.

**Table 6**
Comparison of compliance, maximum von Mises stress, and maximum fatigue damage of the simply supported structure under different load cases and defective lattice materials.

| Micro lattice | Case | Compliance (N·mm) | Max. stress (MPa) | Max. damage |
|---|---|---|---|---|
| Defective lattice 2 | 1 | 0.827 | 171.319 | 0.714 |
| | 2 | 0.768 | 193.236 | 0.805 |
| | 3 | 0.851 | 158.850 | 0.569 |
| | 4 | 0.726 | 186.212 | 1.000 |
| | 5 | 0.819 | 139.669 | 1.000 |
| Defective lattice 3 | 1 | 0.744 | 182.200 | 0.759 |
| | 2 | 0.770 | 165.559 | 0.690 |
| | 3 | 0.819 | 169.822 | 0.608 |
| | 4 | 0.733 | 169.625 | 0.911 |
| | 5 | 0.778 | 139.635 | 1.000 |

Goodman criterion, and its applicability under various fatigue assessment models is validated through the double L-shaped beam example. At the end, the feasibility of the method in solving 3D structural optimization problems is demonstrated using a 3D cantilever beam example.

However, the presented method still has certain limitations that require further investigation. Primarily, the assumption of idealized, deterministic geometric deviations represents a notable limitation for the practical applications of the proposed framework. Since real-world defects in SLM additive manufacturing exhibit strong stochasticity and spatial variability, relying solely on deterministic models cannot completely capture the statistical complexity of actual printed components. To bridge this gap in practical applications, future research could construct a spatially varying stochastic defect database calibrated by experimental data (e.g., CT scan results). By evaluating the equivalent properties of these statistically calibrated unit cells, realistic localized properties can be directly fed into the proposed framework without altering its core optimization mechanism. Beyond the application to defect modeling, the framework's applicability to more challenging engineering scenarios could be enhanced by incorporating cumulative fatigue damage under complex, non-proportional multiaxial loading conditions. Finally, in algorithmic terms, the current optimization relies on a predefined and invariant lattice material configuration. While this decoupled strategy significantly reduces computational costs, it restricts the potential for the microstructure to adapt locally to manufacturing defects. Future work should address this by

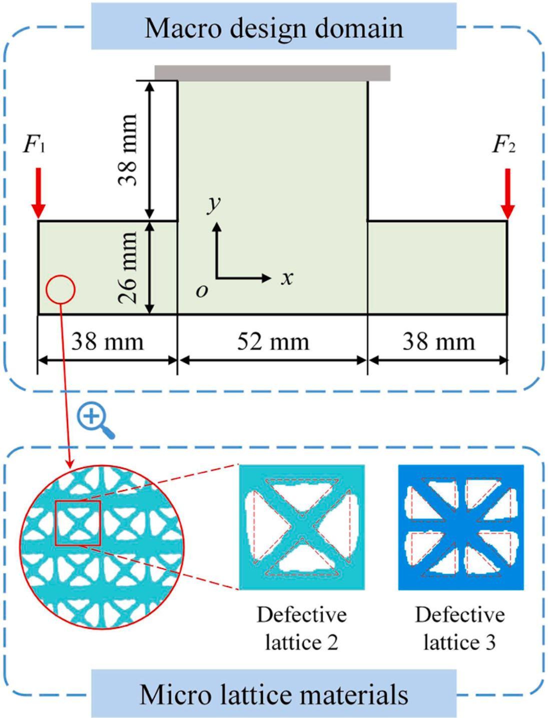


**Fig. 27.** Design domain and boundary conditions of the double L-shaped beam, along with different defective lattice materials.

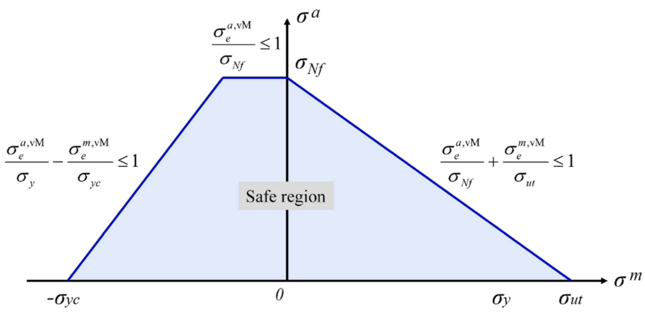


**Fig. 28.** Modified Goodman fatigue diagram.

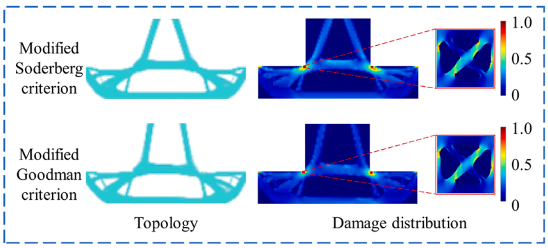


**Fig. 29.** Optimization results of the double L-shaped beam filled with the defective lattice 2.

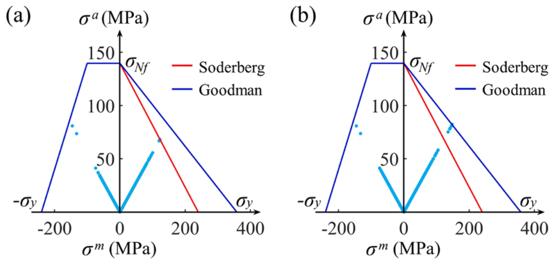


**Fig. 30.** Damage diagrams of the double L-shaped beam filled with the defective lattice 2: (a) modified Soderberg criterion, and (b) modified Goodman criterion.

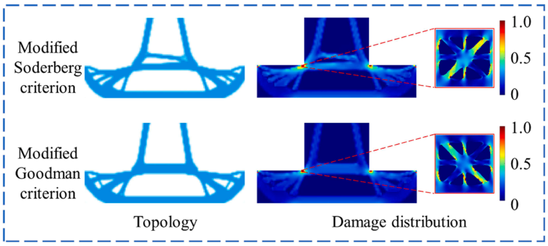


**Fig. 31.** Optimization results of the double L-shaped beam filled with the defective lattice 3.

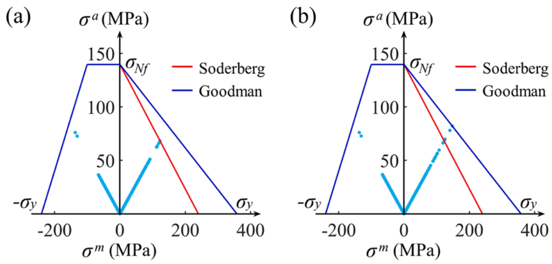


**Fig. 32.** Damage diagrams of the double L-shaped beam filled with the defective lattice 3: (a) modified Soderberg criterion, and (b) modified Goodman criterion.

**Table 7**
Comparison of compliance, maximum von Mises stress, and maximum fatigue damage of the double L-shaped beam under different fatigue criteria and defective lattice materials.

| Micro lattice | Fatigue criterion | Compliance (N·mm) | Max. stress (MPa) | Max. damage |
|---|---|---|---|---|
| Defective lattice 2 | Modified Soderberg | 1.841 | 226.495 | 1.000 |
| | Modified Goodman | 1.840 | 230.421 | 1.003 |
| Defective lattice 3 | Modified Soderberg | 1.706 | 212.832 | 0.999 |
| | Modified Goodman | 1.640 | 229.917 | 1.000 |

implementing concurrent multiscale topology optimization. Such an integrated approach allows the lattice topology itself to evolve in response to defect-induced stress concentrations, thereby unlocking the full potential of defect-tolerant design.

## CRediT authorship contribution statement

**Jinyu Gu:** Writing – original draft, Software, Methodology, Investigation, Funding acquisition, Conceptualization. **Yingjun Wang:** Writing – review & editing, Supervision, Resources, Funding acquisition. **Hang Xu:** Writing – review & editing, Validation, Supervision, Resources, Funding acquisition.

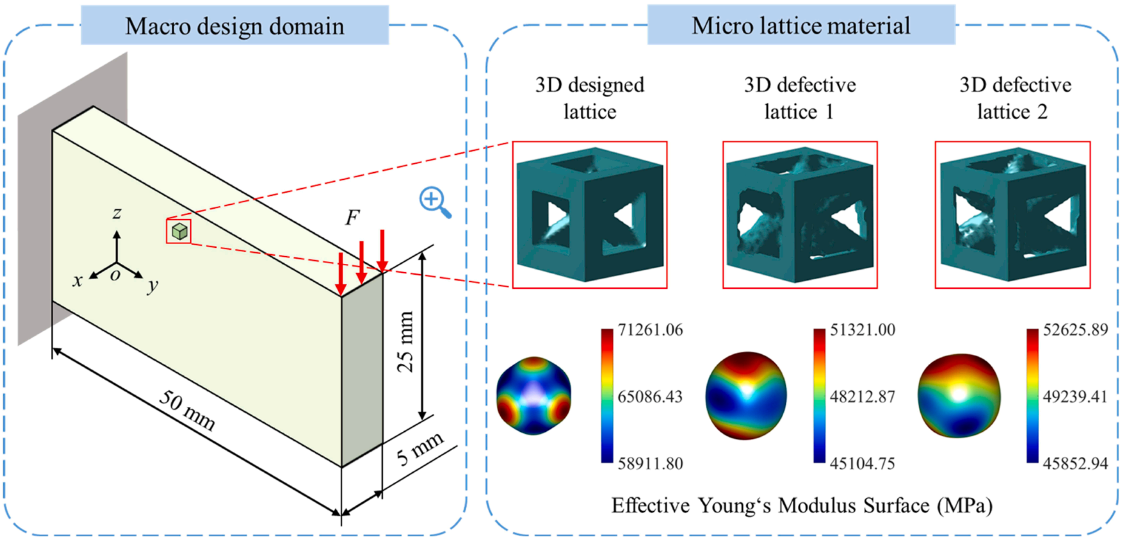


**Fig. 33.** Design domain and boundary conditions of the 3D cantilever beam, along with different micro lattice materials.

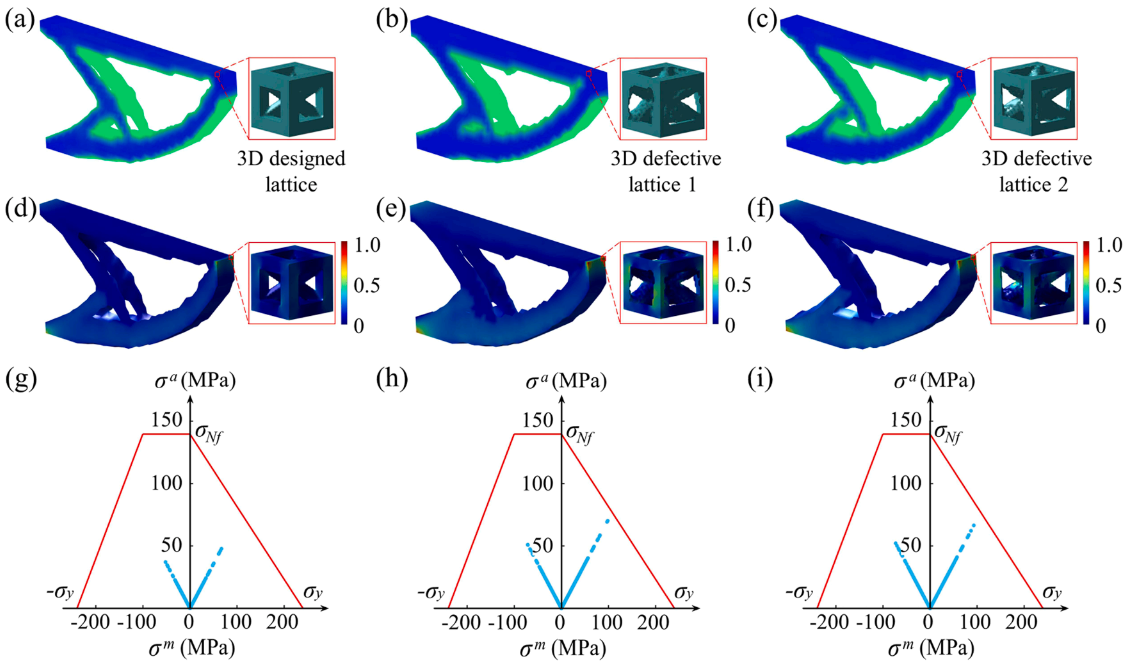


**Fig. 34.** Optimization results of the 3D cantilever beam filled with different micro lattice materials: (a)-(c) topologies; (d)-(f) damage distributions; and (g)-(i) modified Soderberg diagrams. The results correspond to structures composed of the 3D designed lattice (left column), 3D defective lattice 1 (middle column), and 3D defective lattice 2 (right column), respectively.

**Table 8**
Comparison of compliance, maximum von Mises stress, and maximum fatigue damage of the 3D cantilever beam filled with different micro lattice materials.

| Micro lattice | Compliance (N·mm) | Max. stress (MPa) | Max. damage |
|---|---|---|---|
| 3D designed lattice | 0.600 | 114.728 | 0.621 |
| 3D defective lattice 1 | 0.723 | 168.523 | 0.912 |
| 3D defective lattice 2 | 0.741 | 159.626 | 0.864 |

## Declaration of competing interest

The authors declare that they have no known competing financial interests or personal relationships that could have appeared to influence the work reported in this paper.

## Acknowledgments

This work has been supported by the Guangdong Basic and Applied Basic Research Foundation (Grant Nos. 2025A1515010672 and 2024A1515011786) and Natural Sciences and Engineering Research Council of Canada for the financial support of the Discovery Grant (Grant Nos. DGECR-2024–00078 and RGPIN-2024–06567). Besides, the first author gratefully acknowledges the financial support from the China Scholarship Council (CSC) under Grant No. 202406150015.

## Supplementary materials

Supplementary material associated with this article can be found, in the online version, at doi:10.1016/j.cma.2026.118971.

## Appendix A. Sensitivity analysis of the objective and volume constraint functions

The objective function of this study is to minimize the compliance of the macrostructure. The corresponding first-order sensitivity expression with respect to the design variables is given as follows:

$$\frac{\partial c(\boldsymbol{\rho})}{\partial \rho_e^{i,j}} = \frac{\partial c(\boldsymbol{\rho})}{\partial \rho_e} \frac{\partial \rho_e}{\partial \widehat{\rho}_e^{i,j}} \frac{\partial \widehat{\rho}_e^{i,j}}{\partial \rho_e^{i,j}} \tag{A.1}$$

where $\frac{\partial c(\boldsymbol{\rho})}{\partial \rho_e}$ can be derived from Eqs. (32) and (23), as follows:

$$\frac{\partial c(\boldsymbol{\rho})}{\partial \rho_e} = \varsigma(\rho_e)^{\varsigma-1} (\boldsymbol{u}_e)_1^{\mathrm{T}} \left( \int_{\overline{\Omega}_e} \boldsymbol{B}_e^{\mathrm{T}} \boldsymbol{D}_e^{H} \boldsymbol{B}_e |\boldsymbol{J}_1| |\boldsymbol{J}_2| d\overline{\Omega} \right) (\boldsymbol{u}_e)_1 \tag{A.2}$$

The expression for $\frac{\partial \rho_e}{\partial \widehat{\rho}_e^{i,j}} \frac{\partial \widehat{\rho}_e^{i,j}}{\partial \rho_e^{i,j}}$ can be found in Eq. (61). Accordingly, the first-order sensitivity of the objective function with respect to the design variables is given by:

$$\frac{\partial c(\boldsymbol{\rho})}{\partial \rho_e^{i,j}} = \varsigma(\rho_e)^{\varsigma-1} (\boldsymbol{u}_e)_1^{\mathrm{T}} \left( \int_{\overline{\Omega}_e} \boldsymbol{B}_e^{\mathrm{T}} \boldsymbol{D}_e^{H} \boldsymbol{B}_e |\boldsymbol{J}_1| |\boldsymbol{J}_2| d\overline{\Omega} \right) (\boldsymbol{u}_e)_1 \boldsymbol{H}_e \tag{A.3}$$

Similarly, the first-order sensitivity of the volume constraint function with respect to the design variables is given by:

$$\frac{\partial V(\boldsymbol{\rho})}{\partial \rho_e^{i,j}} = v^{\mathrm{mi}} \frac{\partial V(\boldsymbol{\rho})}{\partial \rho_e} \frac{\partial \rho_e}{\partial \widehat{\rho}_e^{i,j}} \frac{\partial \widehat{\rho}_e^{i,j}}{\partial \rho_e^{i,j}} \tag{A.4}$$

$$\frac{\partial V(\boldsymbol{\rho})}{\partial \rho_e} = v_e \tag{A.5}$$

$$\frac{\partial V(\boldsymbol{\rho})}{\partial \rho_e^{i,j}} = v^{\mathrm{mi}} v_e \boldsymbol{H}_e \tag{A.6}$$

## Appendix B. Defective lattice geometry files

The geometric models of the 2D and 3D defective lattices are provided as supplementary files to ensure reproducibility.

## Data availability

Data will be made available on request.

## References

[1] J. Ding, Q. Ma, X. Li, L. Zhang, H. Yang, S. Qu, M.Y. Wang, W. Zhai, H. Gao, X. Song, Imperfection-enabled strengthening of ultra-lightweight lattice materials, Adv. Sci. 11 (2024) 2402727, https://doi.org/10.1002/advs.202402727.

[2] Y. Chi, Y. Gao, M. Akbari, K.H. Yu, K.Y. Wang, M. Patel, S. Fan, Z. Zhang, M. Akbarzadeh, S. Yang, Geometrically templated, ultra-lightweight and high strength soap films from lyotropic liquid crystalline graphene oxide/polymer composites, Adv. Funct. Mater. (2025) e12357, https://doi.org/10.1002/adfm.202512357.
[3] W.W.S. Ma, H. Yang, Y. Zhao, X. Li, J. Ding, S. Qu, Q. Liu, Z. Hu, R. Li, Q. Tao, Multi-physical lattice metamaterials enabled by additive manufacturing: design principles, interaction mechanisms, and multifunctional applications, Adv. Sci. 12 (2025) 2405835, https://doi.org/10.1002/advs.202405835.
[4] D. Gu, X. Shi, R. Poprawe, D.L. Bourell, R. Setchi, J. Zhu, Material-structure-performance integrated laser-metal additive manufacturing, Science 372 (2021) eabg1487, https://doi.org/10.1126/science.abg1487.
[5] N. Khan, A. Riccio, A systematic review of design for additive manufacturing of aerospace lattice structures: current trends and future directions, Prog. Aerosp. Sci. 149 (2024) 101021, https://doi.org/10.1016/j.paerosci.2024.101021.
[6] Z. Li, Y. Luo, M. Lu, Y. Wang, T. Gong, X. He, X. Hu, J. Long, Y. Zhou, L. Min, C. Tu, Biomimetic design and clinical application of Ti-6Al-4V lattice hemipelvis prosthesis for pelvic reconstruction, J. Orthop. Surg. Res. 19 (2024) 210, https://doi.org/10.1186/s13018-024-04672-5.
[7] Q. Guan, B. Dai, H.H. Cheng, J. Hughes, Lattice structure musculoskeletal robots: harnessing programmable geometric topology and anisotropy, Sci. Adv. 11 (2025) eadu9856, https://doi.org/10.1126/sciadv.adu9856.
[8] W. Zhang, J. Xu, Advanced lightweight materials for automobiles: a review, Mater. Des. 221 (2022) 110994, https://doi.org/10.1016/j.matdes.2022.110994.
[9] R. Naboni, A. Kunic, L. Breseghello, Computational design, engineering and manufacturing of a material-efficient 3D printed lattice structure, Int. J. Archit. Comput. 18 (2020) 404–423, https://doi.org/10.1177/1478077120947990.
[10] Z. Leong, R. Chen, Z. Xu, Y. Lin, N. Hu, Robotic arm three-dimensional printing and modular construction of a meter-scale lattice façade structure, Eng. Struct. 290 (2023) 116368, https://doi.org/10.1016/j.engstruct.2023.116368.
[11] Z. Wang, Z. Zhao, P. Bai, J. Ren, B. Liu, N. Naik, B. Liu, H. Qu, The microstructure and property evolutions of Inconel718 lattice structure by selective laser melting, Adv. Compos. Hybrid Mater. 7 (2024) 59, https://doi.org/10.1007/s42114-024-00869-8.
[12] S. Ma, R. Zhu, S. Yang, Q. Yang, K. Wei, Z. Qu, Influence of geometric imperfections on the mechanical behavior for Invar 36 alloy lattice structures fabricated by selective laser melting, Int. J. Mech. Sci. 274 (2024) 109252, https://doi.org/10.1016/j.ijmecsci.2024.109252.
[13] M.R. Khosravani, S. Bieler, K. Weinberg, T. Reinicke, Mechanical fracture of lattice structures fabricated by selective laser sintering, Arch. Civ. Mech. Eng. 25 (2025) 97, https://doi.org/10.1007/s43452-025-01149-y.
[14] N.N.A.A. Abdullah, A.H. Abdullah, M.H. Ramlee, Current trend of lattice structures designed and analysis for porous hip implants: a short review, Mater. Today:. Proc. 110 (2024) 96–100, https://doi.org/10.1016/j.matpr.2023.09.199.
[15] L. Liu, P. Kamm, F. García-Moreno, J. Banhart, D. Pasini, Elastic and failure response of imperfect three-dimensional metallic lattices: the role of geometric defects induced by selective Laser melting, J. Mech. Phys. Solids 107 (2017) 160–184, https://doi.org/10.1016/j.jmps.2017.07.003.
[16] D. Pasini, J.K. Guest, Imperfect architected materials: mechanics and topology optimization, MRS Bull 44 (2019) 766–772, https://doi.org/10.1557/mrs.2019.231.
[17] M. Dallago, B. Winiarski, F. Zanini, S. Carmignato, M. Benedetti, On the effect of geometrical imperfections and defects on the fatigue strength of cellular lattice structures additively manufactured via Selective Laser Melting, Int. J. Fatigue 124 (2019) 348–360, https://doi.org/10.1016/j.ijfatigue.2019.03.019.
[18] S.M. Ahmadi, R. Hedayati, Y. Li, K. Lietaert, N. Tumer, A. Fatemi, C.D. Rans, B. Pouran, H. Weinans, A.A. Zadpoor, Fatigue performance of additively manufactured meta-biomaterials: the effects of topology and material type, Acta Biomater 65 (2018) 292–304, https://doi.org/10.1016/j.actbio.2017.11.014.
[19] M. Benedetti, A. du Plessis, R.O. Ritchie, M. Dallago, N. Razavi, F. Berto, Architected cellular materials: a review on their mechanical properties towards fatigue-tolerant design and fabrication, Mater. Sci. Eng., R 144 (2021) 100606, https://doi.org/10.1016/j.mser.2021.100606.
[20] J. Wei, J. Wang, J. Yang, Y. Zeng, Y. Guan, Effect of internal defects on the compression behavior of stainless steel lattice structure fabricated by selective laser melting, J. Manuf. Processes 120 (2024) 809–826, https://doi.org/10.1016/j.jmapro.2024.04.049.
[21] Z. Xie, X. Fu, Q. Zhang, L. Liu, X. Zhu, Y. Ren, W. Chen, Ballistic performance of additive manufacturing metal lattice structures, Thin-Walled Struct 208 (2025) 112763, https://doi.org/10.1016/j.tws.2024.112763.
[22] R. Zhao, S. Guo, J. Wang, B. Li, F. Zhang, D. Yang, X. Yue, X. Guo, H. Tang, Enhanced energy absorption and mechanical properties of porous Ti-6Al-4 V alloys with gradient disordered cells fabricated by laser powder bed fusion, Thin-Walled Struct 206 (2025) 112632, https://doi.org/10.1016/j.tws.2024.112632.
[23] R. Hedayati, H. Hosseini-Toudeshky, M. Sadighi, M. Mohammadi-Aghdam, A.A. Zadpoor, Computational prediction of the fatigue behavior of additively manufactured porous metallic biomaterials, Int. J. Fatigue 84 (2016) 67–79, https://doi.org/10.1016/j.ijfatigue.2015.11.017.
[24] O. Sigmund, K. Maute, Topology optimization approaches, Struct. Multidiscip. Optim. 48 (2013) 1031–1055, https://doi.org/10.1007/s00158-013-0978-6.
[25] Y. Wang, X. Li, K. Long, P. Wei, Open-source codes of topology optimization: a summary for beginners to start their research, CMES-Comp. Model. Eng. 137 (2023) 1–34, https://doi.org/10.32604/cmes.2023.027603.
[26] J. Gu, T. Gui, Q. Yuan, J. Qu, Y. Wang, Topology optimization method for local relative displacement difference minimization considering stress constraint, Eng. Struct. 304 (2024) 117595, https://doi.org/10.1016/j.engstruct.2024.117595.
[27] F. Lu, K. Long, Y. Diaeldin, A. Saeed, J. Zhang, T. Tao, A time-domain fatigue damage assessment approach for the tripod structure of offshore wind turbines, Sustain Energy Techn 60 (2023) 103450, https://doi.org/10.1016/j.seta.2023.103450.
[28] H. Xie, G. Yang, J. Sun, W. Sai, W. Zeng, Anti-fatigue optimization of the twisting force arm of landing gear based on Kriging approximate sequential optimization method, J. Chin. Inst. Eng. 47 (2024) 1–11, https://doi.org/10.1080/02533839.2023.2274086.
[29] Y. Chen, E. Monteiro, I. Koutiri, V. Favier, Fatigue-constrained topology optimization using the constrained natural element method, Comput. Methods Appl. Mech. Eng. 422 (2024) 116821, https://doi.org/10.1016/j.cma.2024.116821.
[30] S.H. Jeong, D.-H. Choi, G.H. Yoon, Fatigue and static failure considerations using a topology optimization method, Appl. Math. Modell. 39 (2015) 1137–1162, https://doi.org/10.1016/j.apm.2014.07.020.
[31] Z. Chen, K. Long, C. Zhang, X. Yang, F. Lu, R. Wang, B. Zhu, X. Zhang, A fatigue-resistance topology optimization formulation for continua subject to general loads using rainflow counting, Struct. Multidiscip. Optim. 66 (2023) 210, https://doi.org/10.1007/s00158-023-03658-x.
[32] B. Desmorat, R. Desmorat, Topology optimization in damage governed low cycle fatigue, C.R. Mecanique 336 (2008) 448–453, https://doi.org/10.1016/j.crme.2008.01.001.
[33] L. Zhao, B. Xu, Y. Han, J. Xue, J. Rong, Structural topological optimization with dynamic fatigue constraints subject to dynamic random loads, Eng. Struct. 205 (2020) 110089, https://doi.org/10.1016/j.engstruct.2019.110089.
[34] K. Nabaki, J. Shen, X. Huang, Effect of different fatigue constraints on optimal topology of structures with minimum weight, Eng. Struct. 288 (2023) 116149, https://doi.org/10.1016/j.engstruct.2023.116149.
[35] T. Zhao, Y. Zhang, Y. Ou, W. Ding, F. Cheng, Fail-safe topology optimization considering fatigue, Struct. Multidiscip. Optim. 66 (2023) 132, https://doi.org/10.1007/s00158-023-03588-8.
[36] J. Gu, J. Yang, Y. Wang, High-cycle fatigue-constrained isogeometric topology optimization, Thin-Walled Struct 209 (2025) 112907, https://doi.org/10.1016/j.tws.2025.112907.
[37] Z. Ni, W. Cheng, Y. Wang, Y. Luo, X. Zhang, Z. Kang, Topology optimization of two-scale hierarchical structures with high-cycle fatigue resistance, Comput. Methods Appl. Mech. Eng. 430 (2024) 117213, https://doi.org/10.1016/j.cma.2024.117213.
[38] J. Gu, Z. Chen, K. Long, Y. Wang, Nonlinear fatigue damage constrained topology optimization, Comput. Methods Appl. Mech. Eng. 429 (2024) 117136, https://doi.org/10.1016/j.cma.2024.117136.
[39] J.W. Lee, G.H. Yoon, S.H. Jeong, Topology optimization considering fatigue life in the frequency domain, Comput. Math. Appl. 70 (2015) 1852–1877, https://doi.org/10.1016/j.camwa.2015.08.006.
[40] H. Ye, Z. Li, N. Wei, P. Su, Y. Sui, Fatigue topology optimization design based on distortion energy theory and independent continuous mapping method, CMES-Comp. Model. Eng. 128 (2021) 297–314, https://doi.org/10.32604/cmes.2021.016133.
[41] C. Wang, W. Zhang, Finite-life fatigue constrained topology optimization for self-supporting structures in additive manufacturing, Comput. Methods Appl. Mech. Eng. 436 (2025) 117728, https://doi.org/10.1016/j.cma.2024.117728.

[42] D. Zhao, H. Wang, Topology optimization of compliant mechanisms considering manufacturing uncertainty, fatigue, and static failure constraints, Processes 11 (2023) 2914, https://doi.org/10.3390/pr11102914.
[43] S.M. Hermansen, E. Lund, Multi-material and thickness optimization of laminated composite structures subject to high-cycle fatigue, Struct. Multidiscip. Optim. 66 (2023) 259, https://doi.org/10.1007/s00158-023-03708-4.
[44] J. Wu, O. Sigmund, J.P. Groen, Topology optimization of multi-scale structures: a review, Struct. Multidiscip. Optim. 63 (2021) 1455–1480, https://doi.org/10.1007/s00158-021-02881-8.
[45] M. Zhou, L. Gao, M. Xiao, X. Liu, M. Huang, Multiscale topology optimization of cellular structures using Nitsche-type isogeometric analysis, Int. J. Mech. Sci. 256 (2023) 108487, https://doi.org/10.1016/j.ijmecsci.2023.108487.
[46] A. Nale, A. Chiozzi, Multiscale topology optimization with embedded TPMS architected materials, Int. J. Mech. Sci. 295 (2025), https://doi.org/10.1016/j.ijmecsci.2025.110204.
[47] J. Feng, L. Wang, X. Zhai, K. Chen, W. Wu, L. Liu, X.-M. Fu, Constructing boundary-identical microstructures via guided diffusion for fast multiscale topology optimization, Comput. Methods Appl. Mech. Eng. 436 (2025) 117735, https://doi.org/10.1016/j.cma.2025.117735.
[48] M.A. Ali, M. Shimoda, Toward multiphysics multiscale concurrent topology optimization for lightweight structures with high heat conductivity and high stiffness using MATLAB, Struct. Multidiscip. Optim. 65 (2022) 207, https://doi.org/10.1007/s00158-022-03291-0.
[49] J. Wang, Q. Zhang, Y. Zhang, Y. Wang, W.-H. Liao, Q. Gao, Multiscale concurrent topology optimization considering transient heat conduction under coupled thermo-mechanical loads, Aerosp. Sci. Technol. 165 (2025) 110508, https://doi.org/10.1016/j.ast.2025.110508.
[50] J. Gao, Z. Luo, H. Li, P. Li, L. Gao, Dynamic multiscale topology optimization for multi-regional micro-structured cellular composites, Compos. Struct. 211 (2019) 401–417, https://doi.org/10.1016/j.compstruct.2018.12.031.
[51] X. Liu, L. Gao, M. Xiao, An efficient multiscale topology optimization method for frequency response minimization of cellular composites, Eng. Comput-Germany 41 (2024) 267–291, https://doi.org/10.1007/s00366-024-02000-3.
[52] C.F. Christensen, F. Wang, O. Sigmund, Topology optimization of multiscale structures considering local and global buckling response, Comput. Methods Appl. Mech. Eng. 408 (2023) 115969, https://doi.org/10.1016/j.cma.2023.115969.
[53] M.-N. Nguyen, D. Lee, Buckling-constrained and stress-based multi-material topology optimization framework for thermoelastic and self-weight structures, Eng. Comput-Germany (2025), https://doi.org/10.1007/s00366-025-02209-w.
[54] T.J.R. Hughes, J.A. Cottrell, Y. Bazilevs, Isogeometric analysis: CAD, finite elements, NURBS, exact geometry and mesh refinement, Comput. Methods Appl. Mech. Eng. 194 (2005) 4135–4195, https://doi.org/10.1016/j.cma.2004.10.008.
[55] V.N.V. Do, T.H. Ong, C.-H. Lee, Isogeometric analysis for nonlinear buckling of FGM plates under various types of thermal gradients, Thin-Walled Struct. 137 (2019) 448–462, https://doi.org/10.1016/j.tws.2019.01.024.
[56] Y. Wang, M. Xiao, Z. Xia, P. Li, L. Gao, From computer-aided design (CAD) toward human-aided design (HAD): an isogeometric topology optimization approach, Engineering 22 (2023) 94–105, https://doi.org/10.1016/j.eng.2022.07.013.
[57] L. Yang, W. Wang, Y. Ji, C.-G. Zhu, C.C.L. Wang, Space–time isogeometric topology optimization with additive manufacturing constraints, Comput. Methods Appl. Mech. Eng. 441 (2025) 117976, https://doi.org/10.1016/j.cma.2025.117976.
[58] Y. Wang, H. Xu, D. Pasini, Multiscale isogeometric topology optimization for lattice materials, Comput. Methods Appl. Mech. Eng. 316 (2017) 568–585, https://doi.org/10.1016/j.cma.2016.08.015.
[59] J. Gao, M. Xiao, Y. Zhang, L. Gao, A comprehensive review of isogeometric topology optimization: methods, applications and prospects, Chin. J. Mech. Eng-EN 33 (2020) 87, https://doi.org/10.1186/s10033-020-00503-w.
[60] J. Liu, H. Fan, T. Nie, H. Zhang, J. Yu, S. Wang, Z. Xia, Multi-objective concurrent isogeometric topology optimization of multiscale structures, Front. Mech. Eng. 20 (2025) 4, https://doi.org/10.1007/s11465-024-0819-x.
[61] B. Van Hooreweder, Y. Apers, K. Lietaert, J.P. Kruth, Improving the fatigue performance of porous metallic biomaterials produced by Selective Laser Melting, Acta Biomater 47 (2017) 193–202, https://doi.org/10.1016/j.actbio.2016.10.005.
[62] A. Moussa, D. Melancon, A. El Elmi, D. Pasini, Topology optimization of imperfect lattice materials built with process-induced defects via powder bed fusion, Addit. Manuf. 37 (2021) 101608, https://doi.org/10.1016/j.addma.2020.101608.
[63] O. Sigmund, Manufacturing tolerant topology optimization, Acta Mech. Sin. 25 (2009) 227–239, https://doi.org/10.1007/s10409-009-0240-z.
[64] B. Liu, C. Jiang, G. Li, X. Huang, Topology optimization of structures considering local material uncertainties in additive manufacturing, Comput. Methods Appl. Mech. Eng. 360 (2020) 112786, https://doi.org/10.1016/j.cma.2019.112786.
[65] V.P. Nguyen, C. Anitescu, S.P. Bordas, T. Rabczuk, Isogeometric analysis: an overview and computer implementation aspects, Math. Comput. Simul 117 (2015) 89–116, https://doi.org/10.1016/j.matcom.2015.05.008.
[66] Y. Wang, D.J. Benson, Isogeometric analysis for parameterized LSM-based structural topology optimization, Comput. Mech. 57 (2016) 19–35, https://doi.org/10.1007/s00466-015-1219-1.
[67] P. Fischer, M. Klassen, J. Mergheim, P. Steinmann, R. Müller, Isogeometric analysis of 2D gradient elasticity, Comput. Mech. 47 (2010) 325–334, https://doi.org/10.1007/s00466-010-0543-8.
[68] D. Rypl, B. Patzák, From the finite element analysis to the isogeometric analysis in an object oriented computing environment, Adv. Eng. Software 44 (2012) 116–125, https://doi.org/10.1016/j.advengsoft.2011.05.032.
[69] A. Norouzzadeh, R. Ansari, A comprehensive comparative study on the nonlinear finite element and isogeometric analyses of shell-type structures, Int. J. Numer. Methods Eng. 126 (2025) e70180, https://doi.org/10.1002/nme.70180.
[70] W. Qiu, Q. Wang, L. Gao, Z. Xia, Stress-based evolutionary topology optimization via XIGA with explicit geometric boundaries, Int. J. Mech. Sci. 256 (2023) 108512, https://doi.org/10.1016/j.ijmecsci.2023.108512.
[71] K. Nabaki, J. Shen, X. Huang, Evolutionary topology optimization of continuum structures considering fatigue failure, Mater. Des. 166 (2019) 107586, https://doi.org/10.1016/j.matdes.2019.107586.
[72] R. Pawliczek, D. Rozumek, The effect of mean load for S355J0 steel with increased strength, Metals (Basel) 10 (2020) 209, https://doi.org/10.3390/met10020209.
[73] B. Hassani, E. Hinton, A review of homogenization and topology optimization I—Homogenization theory for media with periodic structure, Comput. Struct. 69 (1998) 707–717, https://doi.org/10.1016/S0045-7949(98)00131-X.
[74] E. Andreassen, C.S. Andreasen, How to determine composite material properties using numerical homogenization, Comput. Mater. Sci 83 (2014) 488–495, https://doi.org/10.1016/j.commatsci.2013.09.006.
[75] G. Dong, Y. Tang, Y.F. Zhao, International Journal of Fatigue, J. Eng. Mater. Technol. 141 (2019) 011005, https://doi.org/10.1115/1.4040555.
[76] Z.S. Bagheri, D. Melancon, L. Liu, R.B. Johnston, D. Pasini, Compensation strategy to reduce geometry and mechanics mismatches in porous biomaterials built with Selective Laser Melting, J. Mech. Behav. Biomed. Mater. 70 (2017) 17–27, https://doi.org/10.1016/j.jmbbm.2016.04.041.
[77] E. Andreassen, A. Clausen, M. Schevenels, B.S. Lazarov, O. Sigmund, Efficient topology optimization in MATLAB using 88 lines of code, Struct. Multidiscip. Optim. 43 (2010) 1–16, https://doi.org/10.1007/s00158-010-0594-7.
[78] F. Wang, B.S. Lazarov, O. Sigmund, On projection methods, convergence and robust formulations in topology optimization, Struct. Multidiscip. Optim. 43 (2011) 767–784, https://doi.org/10.1007/s00158-010-0602-y.
[79] J. Panetta, A. Rahimian, D. Zorin, Worst-case stress relief for microstructures, ACM Trans. Graphics 36 (2017) 1–16, https://doi.org/10.1145/3072959.3073649.
[80] R. Zhao, J. Zhao, C. Wang, Stress-constrained multiscale topology optimization with connectable graded microstructures using the worst-case analysis, Int. J. Numer. Methods Eng. 123 (2022) 1882–1906, https://doi.org/10.1002/nme.6920.
[81] Z. Chen, K. Long, P. Wen, S. Nouman, Fatigue-resistance topology optimization of continuum structure by penalizing the cumulative fatigue damage, Adv. Eng. Software 150 (2020) 102924, https://doi.org/10.1016/j.advengsoft.2020.102924.

[82] Y. Han, B. Xu, Z. Duan, X. Huang, Stress-based bi-directional evolutionary structural topology optimization considering nonlinear continuum damage, Comput. Methods Appl. Mech. Eng. 396 (2022) 115086, https://doi.org/10.1016/j.cma.2022.115086.
[83] C. Le, J. Norato, T. Bruns, C. Ha, D. Tortorelli, Stress-based topology optimization for continua, Struct. Multidiscip. Optim. 41 (2009) 605–620, https://doi.org/10.1007/s00158-009-0440-y.
[84] J.A. Norato, H.A. Smith, J.D. Deaton, R.M. Kolonay, A maximum-rectifier-function approach to stress-constrained topology optimization, Struct. Multidiscip. Optim. 65 (2022) 286, https://doi.org/10.1007/s00158-022-03357-z.
[85] M. Kočvara, M. Stingl, Solving stress constrained problems in topology and material optimization, Struct. Multidiscip. Optim. 46 (2012) 1–15, https://doi.org/10.1007/s00158-012-0762-z.
[86] E. Holmberg, B. Torstenfelt, A. Klarbring, Stress constrained topology optimization, Struct. Multidiscip. Optim. 48 (2013) 33–47, https://doi.org/10.1007/s00158-012-0880-7.
[87] K. Svanberg, The method of moving asymptotes—A new method for structural optimization, Int. J. Numer. Methods Eng. 24 (1987) 359–373, https://doi.org/10.1002/nme.1620240207.
[88] K.-T. Zuo, L.-P. Chen, Y.-Q. Zhang, J. Yang, Study of key algorithms in topology optimization, Int. J. Adv. Manuf. Tech. 32 (2006) 787–796, https://doi.org/10.1007/s00170-005-0387-0.